

# Numerical Methods for a Poisson-Nernst-Planck-Fermi Model

Jinn-Liang Liu

*Department of Applied Mathematics, National Hsinchu University of Education,  
Hsinchu 300, Taiwan (jinnliu@mail.nhcue.edu.tw)*

Bob Eisenberg

*Department of Molecular Biophysics and Physiology, Rush University, Chicago, IL  
60612 USA (beisenbe@rush.edu)*

---

**Abstract.** Numerical methods are proposed for an advanced Poisson-Nernst-Planck-Fermi (PNPF) model for studying ion transport through biological ion channels. PNPF contains many more correlations than most models and simulations of channels, because it includes water and calculates dielectric properties consistently as outputs. This model accounts for the steric effect of ions and water molecules with different sizes and interstitial voids, the correlation effect of crowded ions with different valences, and the screening effect of polarized water molecules in an inhomogeneous aqueous electrolyte. The steric energy is shown to be comparable to the electrical energy under physiological conditions, demonstrating the crucial role of the excluded volume of particles and the voids in the natural function of channel proteins. Water is shown to play a critical role in both correlation and steric effects in the model. We extend the classical Scharfetter-Gummel (SG) method for semiconductor devices to include the steric potential for ion channels, which is a fundamental physical property not present in semiconductors. Together with a simplified matched interface and boundary (SMIB) method for treating molecular surfaces and singular charges of channel proteins, the extended SG method is shown to exhibit important features in flow simulations such as optimal convergence, efficient nonlinear iterations, and physical conservation. The generalized SG stability condition shows why the standard discretization (without SG exponential fitting) of NP equations may fail and that divalent  $\text{Ca}^{2+}$  may cause more unstable discrete  $\text{Ca}^{2+}$  fluxes than that of monovalent  $\text{Na}^+$ . Two different methods — called the SMIB and multiscale methods — are proposed for two different types of channels, namely, the gramicidin A channel and an L-type calcium channel, depending on whether water is allowed to pass through the channel. Numerical methods are first validated with constructed

models whose exact solutions are known. The experimental data of both channels are then used to verify and explain novel features of PNPF as compared with previous PNP models. The PNPF currents are in accord with the experimental I-V (V for applied voltages) data of the gramicidin A channel and I-C (C for bath concentrations) data of the calcium channel with  $10^{-8}$ -fold bath concentrations that pose severe challenges in theoretical simulations.

PACS number(s): 87.10.Ed 02.70.-c 47.61.Cb 05.20.Jj

## I. INTRODUCTION

The literature on numerical methods for drift-diffusion (DD) or Poisson-Nernst-Planck (PNP) models of semiconductor devices and ion channels is large, including [1,2,3,4,5,6,7,8,9,10,11,12,13,14,15,16,17,18,19,20,21,22] and references therein. In biological simulations, continuum models have been challenged as inaccurate compared to Monte Carlo (MC), Brownian dynamics (BD), or molecular dynamics (MD) due to the gross approximation of atomic properties of channel proteins and electrolyte solutions [23,24,25,26,27,28,29,30,31,32,33]. Continuum models on the other hand have substantial advantages in efficiency that are of great importance in studying a range of conditions and concentrations especially for large nonequilibrium or inhomogeneous systems, as are present in experiments and in life itself [15,20,21,22,28,34,35,36,37,38,39,40,41].

Based on the configurational entropy model [42] for aqueous electrolytes with arbitrary  $K$  species of nonuniform size, hard spherical ions, we extended the Poisson-Fermi model in [42] to a new model — called the Poisson-Nernst-Planck-Fermi (PNPF) model — for nonequilibrium systems by including specifically the excluded volume effects of the next species ( $K+1$ ) of water molecules and the interstitial voids ( $K+2$ ) between all particles [43]. The PNPF model differs from most channel models in several respects: (i) it computes dielectric properties as an output that in fact vary with position and with experimental condition, (ii) a fourth order Cahn-Hilliard type partial differential equation emerges to replace the second order Poisson equation of PNP, which has a richness of behavior beyond the usual second order PNP description, and (iii) using the methods of this paper, this more powerfully correlated model is in fact much easier to compute in three dimensions than other steric PNP models. Previous work [43] gives more details.

The PNPF model also provides a quantitative mean-field description of the charge/space competition mechanism of particles within the highly charged and crowded channel pore. The steric energy lumps the effects of excluded volumes of all ions, water, and voids. It yields an energy landscape of ions that varies significantly with bath concentrations in a  $10^8$ -fold range of experimental conditions for L-type calcium channels.

**Computational Challenges.** The  $10^8$ -fold range of bath conditions and the highly energetic behavior of permeating ions through the extremely crowded narrow channels pose severe challenges in implementations. The strength of local electric fields in a calcium channel can be higher than that in a semiconductor device (comparing, for example, 0.27 V/nm estimated from Fig. 13 in this paper for ion channel and 0.06 V/nm from Fig. 7 in [18] for semiconductor device). This means that the convergence and stability problems in ion channel simulation can be more severe than those in semiconductor devices. These problems are not made easier by the presence of countervailing steric potentials of the same order of magnitude.

Moreover, geometric complexity and singularities of molecular surfaces separating electrolyte solutions from protein atoms in biological systems need to be carefully treated in order to obtain tolerable accuracy in 3D PNP simulations [22]. Seemingly small numerical over approximations can lead to errors that make results not useful. A second-order method called the matched interface and boundary (MIB) method was developed by Wei et al. [22,44] for Poisson-Boltzmann and PNP models and is simplified (SMIB) in [45] for the PF model to deal with the geometric singularities by the standard finite difference approximation.

The Scharfetter-Gummel (SG) [2] method is an *optimal* and uniformly convergent method (with respect to the mesh size) to discretize drift-diffusion (or Nernst-Planck) equations for flux calculations because it integrates the corresponding 1D initial value problem *exactly* at *every* grid point [5]. We extend the classical SG method to the NPF equation by showing how the Fermi distribution of hard spheres of water and ions is imposed. If the classical Boltzmann distribution is used, the density of point charges would grossly overestimate ionic concentrations (that are in fact limited because of the finite size of ions) and consequently lead to inaccurate electrostatic potential and ion mobility by the classical PNP [25,29,35]. We also show that the classical Goldman-Hodgkin-Katz flux approximation [46] in ion channels is in fact exactly the Scharfetter-Gummel flux approximation on grid points in semiconductor devices. Similar results appear in the seminal work of Mott [47] that was well known to Hodgkin, Cole, and Goldman. The pioneers in two different fields had the same idea that made a profound impact on their respective fields and others.

The SG stability condition — a critical condition of the flux equation in implementation — is also extended to include the steric potential that is not present in classical PNP models. This stability condition explains why the standard finite difference or finite element discretization fails when the electric and/or steric potentials vary sharply in a layer region and the mesh of grid points is not sufficiently resolved. It plays a key role in preserving physically positive concentrations and divergence-free currents (current conservation) in

approximation [10]. We take a closer look at the numerics concerning the extended SG condition and discover that this condition is harder to satisfy for the standard methods for the divalent  $\text{Ca}^{2+}$  than the monovalent  $\text{Na}^+$  flux since the SG condition depends on the valence of ions. This is physically reasonable because  $\text{Ca}^{2+}$  ions are more energetic in binding and permeation in voltage-gated calcium channels that conduct  $\text{Ca}^{2+}$  ions with high-fidelity and high-throughput [48].

The combined method — the SMIB-SG method — is shown not only to achieve second order of accuracy for the PNPF model (with constructed exact solutions) but also to outperform the primitive SMIB method (without SG) for the gramicidin A channel due to the exactness property of the SG exponential fitting between grid points. We also show that the primitive SMIB method fails to converge for the calcium channel due to its highly charged ( $-4e$ ,  $e$  is the proton charge) and very narrow (about 1 Å in radius) binding site as compared with that of the gramicidin A channel ( $-2e$  and about 2 Å in radius). In our simulations, water (1.4 Å in radius) is found to flow through the gramicidin A channel but not to flow through the calcium channel in some conditions. We use a second method — called the multiscale method — that treats water and ions explicitly in the binding site of the calcium channel so that water may not move through the channel. It is multiscale since both Poisson’s theory of continuous charges and Coulomb’s law of discrete charges are used in the solvent domain. This demonstrates the novelty of the PNPF model as compared with previous PNP models in dealing with ion-protein, ion-ion, and ion-water interactions and the steric effect of ions and water in the narrow pore. PNPF captures many more of the correlations not present in PNP itself. It captures steric interactions of ions and water and packs them well (i.e. consistently) because it includes free space. Dielectric properties vary with position and concentration and are fully consistent with the rest of the model because they are outputs of the calculations, not inputs, as assumed in most channel models.

The nonlinear algebraic systems of discrete PNP equations are very difficult to solve due to strong nonlinearity of the coupled system in both semiconductor devices and ion channels, especially with sharp potentials at practical applied voltages [5,9,10,14,15,16,18,19,20,21,22]. The PNPF model consists of  $K + 2$  PDEs (1 fourth-order Poisson-Fermi and  $K + 1$  second-order Nernst-Planck). The fourth-order PF equation was proposed to account for the correlation effect of ions in water [49] and transformed to two second-order PDEs for computational efficiency and for calculating variable permittivity within the channel pore [42,45]. The last NP equation describes the dynamics of water molecules that play a critical role not only in the steric arrangement of all particles but also in its screening and polarization effects on ions in the system [42,45]. The full PNPF model incorporates these atomic properties and thus can provide more accurate simulations but obviously at the expense of

more difficulties in implementation than that of previous PNP models. It is impractical to solve the  $(K + 2)M$  nonlinear algebraic equations resulting from a discretization of PNPF using Newton's iteration on the coupled system, where the matrix size  $M$  corresponding to each PDE can easily grow to millions in 3D implementations. With a linearized Poisson equation, Gummel's iteration is an efficient method because it solves each PDE successively [9]. It has been shown in [22] that an SOR-like method (without linearization) converges faster than Gummel's method at higher bath concentrations for ion channel simulations provided that the relaxation parameter is appropriately chosen. We present a new SOR-like method for the PNPF model that differs from the previous models in the fourth-order PDE, the water NP equation, and the steric potential. It is shown that the method improves the convergence rate using the same gramicidin A channel protein as considered in [22].

The rest of the paper is organized as follows. In Section 2, we briefly describe the PNPF theory. Sections 3 and 4 present the numerical methods proposed in this paper. Section 4 also include two algorithms with respect to the SMIB and multiscale methods to illustrate implementation procedures for studying two different types of ion channels. In Section 5, the SMIB and SG methods are first validated by using a real protein structure of the GA channel with a set of exact solutions constructed for the PNP model. Both methods are shown to achieve optimal results as analyzed in this paper. The extended SG condition is then carefully scrutinized in discretization and used to explain why the standard discretization method is not feasible for the calcium channel model considered here, especially to approximate the high energetic  $\text{Ca}^{2+}$  flux. PNPF results are shown to agree with experimental I-V and I-C data of GA and calcium channels using the two algorithms, respectively. Some concluding remarks are made in Section 6.

## II. POISSON-NERNST-PLANCK-FERMI MODEL

For an electrolyte in a solvent domain  $\Omega_s$  with arbitrary  $K$  species of ions and the next species  $K + 1$  of water, the configurational entropy model proposed in [42] is extended in [43] to treat all particles as hard spheres with nonuniform sizes and to include explicitly as its last species  $K + 2$  the voids between all particles. Based on the extended entropy model, the following Gibbs-Fermi free energy functional of the system is proposed in [43]

$$G^{\text{Fermi}} = \int_{\Omega_s} d\mathbf{r} \left\{ -\frac{\epsilon_s l_c^2}{2} \left( \nabla^2 \phi(\mathbf{r}) \right)^2 - \frac{\epsilon_s}{2} |\nabla \phi(\mathbf{r})|^2 + \rho(\mathbf{r}) \phi(\mathbf{r}) + g \right\} \quad (1)$$

$$g = k_B T \left( \sum_{j=1}^{K+1} \left[ C_j(\mathbf{r}) \ln(v_j C_j(\mathbf{r})) - C_j(\mathbf{r}) \right] - C_{K+2}(\mathbf{r}) \ln(v_{K+2} C_{K+2}(\mathbf{r})) - \frac{\mu_i^B C_j(\mathbf{r})}{k_B T} \right),$$

where  $\epsilon_s = \epsilon_w \epsilon_0$ ,  $\epsilon_w$  is the dielectric constant of bulk water,  $\epsilon_0$  is the vacuum

permittivity,  $l_c$  is a correlation length [49,50],  $\phi(\mathbf{r})$  is the electrostatic potential function of spatial variable  $\mathbf{r} \in \Omega_s$ ,  $\rho(\mathbf{r}) = \sum_{j=1}^{K+1} q_j C_j(\mathbf{r})$  is the charge density,  $C_j(\mathbf{r})$  is the concentration of type  $j$  particles carrying the charge  $q_j = z_j e$  with valence  $z_j$  and having the volume  $v_j = 4\pi a_j^3/3$  with radius  $a_j$ ,  $k_B$  is the Boltzmann constant,  $T$  is the absolute temperature, and  $\mu_i^B = k_B T \ln(v_i C_i^B/\Gamma^B)$  is a constant chemical potential. Water is treated as polarizable spheres with zero net charge, so  $z_{K+1} = q_{K+1} = 0$ .

The total volume  $V$  of the system consists of the volumes of all particles and the total void volume  $v_{K+2}$ , i.e.,  $V = \sum_{j=1}^{K+1} v_j N_j + v_{K+2}$ , where  $N_j$  is the total number of type  $j$  particles. Under the bulk condition, dividing this equation by  $V$  yields the bath void volume fraction

$$\Gamma^B = \frac{v_{K+2}}{V} = 1 - \sum_{j=1}^{K+1} v_j \frac{N_j}{V} = 1 - \sum_{j=1}^{K+1} v_j C_j^B, \quad (2)$$

where  $C_j^B$  is the bath concentration. The void fraction function

$$\Gamma(\mathbf{r}) = 1 - \sum_{j=1}^{K+1} v_j C_j(\mathbf{r}) = v_{K+2} C_{K+2}(\mathbf{r}), \quad (3)$$

varies with concentrations  $C_j(\mathbf{r})$  of all particles and thus with the distribution  $C_{K+2}(\mathbf{r})$  of interstitial voids.

Minimizing the Gibbs-Fermi functional (1) with respect to  $\phi$  and  $C_i$  yields the Poisson-Fermi equation [42,45,49,50]

$$\epsilon_s (l_c^2 \nabla^2 - 1) \nabla^2 \phi(\mathbf{r}) = \sum_{i=1}^K q_i C_i(\mathbf{r}) = \rho(\mathbf{r}) \quad (4)$$

and the Fermi distribution

$$C_i(\mathbf{r}) = C_i^B \exp(-\beta_i \phi(\mathbf{r}) + S^{\text{trc}}(\mathbf{r})), \quad S^{\text{trc}}(\mathbf{r}) = \ln \frac{\Gamma(\mathbf{r})}{\Gamma^B}, \quad (5)$$

respectively, where  $\beta_i = q_i/(k_B T)$  and  $S^{\text{trc}}(\mathbf{r})$  is called the steric potential. The fourth-order PF equation reduces to the classical Poisson-Boltzmann (PB) equation  $-\epsilon_s \nabla^2 \phi = \rho$  and the Fermi distribution reduces to the Boltzmann distribution  $C_i = C_i^B \exp(-\beta_i \phi)$  when  $l_c = S^{\text{trc}}(\mathbf{r}) = 0$ . The distribution (5) is of Fermi type since all concentration functions are bounded above,  $C_i(\mathbf{r}) < 1/v_i$  [43], i.e.,  $C_i(\mathbf{r})$  cannot exceed the maximum value  $1/v_i$  for any arbitrary (or even infinite) potential  $\phi(\mathbf{r})$  at any location  $\mathbf{r}$  in the domain  $\Omega_s$ .

If  $l_c \neq 0$ , the dielectric operator  $\hat{\epsilon} = \epsilon_s(1 - l_c^2 \nabla^2)$  approximates the permittivity of the bulk solvent and the linear response of correlated ions [50]. The dielectric function  $\tilde{\epsilon}(\mathbf{r}) = \epsilon_w/(1 + \eta/\rho)$  is a further approximation of  $\hat{\epsilon}$ . It is found by

transforming (4) into two second-order PDEs [45]

$$\text{PF1} : \epsilon_s (l_c^2 \nabla^2 - 1) \Psi(\mathbf{r}) = \rho(\mathbf{r}) \quad (6)$$

$$\text{PF2} : \nabla^2 \phi(\mathbf{r}) = \Psi(\mathbf{r}) \quad (7)$$

by introducing a density like variable  $\Psi$  that yields a polarization charge density  $\eta = -\epsilon_s \Psi - \rho$  of water using Maxwell's first equation [42]. Numerical approximation of the fourth order equation (4) was simplified to the standard 7-point finite difference approximation of the second order equations (6) and (7) in [45]. Boundary conditions of the new variable  $\Psi$  on the solvent boundary  $\partial\Omega_s$  were derived from the global charge neutrality condition [45]. These functions make dielectric properties outputs in our model and calculations, unlike in most other treatments of channels.

Including the electrostatic effect of a total of  $Q$  fixed atomic charges  $q_j$  located at  $\mathbf{r}_j$  in the biomolecular domain  $\Omega_m$  that contains both channel protein and membrane lipids, the PF equation (4) is written as

$$\epsilon (l_c^2 \nabla^2 - 1) \nabla^2 \phi(\mathbf{r}) = \sum_{j=1}^Q q_j \delta(\mathbf{r} - \mathbf{r}_j) + \sum_{i=1}^K q_i C_i(\mathbf{r}) = \rho(\mathbf{r}), \forall \mathbf{r} \in \Omega, \quad (8)$$

where  $\Omega = \Omega_s \cup \Omega_m$  and  $\delta(\mathbf{r} - \mathbf{r}_j)$  is the delta function. Note that  $\epsilon = \epsilon_m \epsilon_0$ ,  $l_c = 0$ ,  $\rho(\mathbf{r}) = \sum_{j=1}^Q q_j \delta(\mathbf{r} - \mathbf{r}_j)$  in  $\Omega_m$  and  $\epsilon = \epsilon_s \epsilon_0$ ,  $l_c \neq 0$ ,  $\rho(\mathbf{r}) = \sum_{i=1}^K q_i C_i(\mathbf{r})$  in  $\Omega_s$ , where  $\epsilon_m$  is the dielectric constant of biomolecules. As mentioned above, numerical implementation of Eq. (8) (or Eqs. (6) and (7)) is complicated by the complex molecular surface  $\partial\Omega_m$  in real protein structures on which suitable interface conditions for the unknown functions  $\Psi(\mathbf{r})$  and  $\phi(\mathbf{r})$  should be properly imposed [45]. The approximation of interface conditions is not straightforward [22,44,45] and can be made much worse by geometric singularities of  $\partial\Omega_m$  if the singularities are not properly treated. It was shown in [51] that the standard, second-order finite difference method is degraded to only  $O(h^{0.37})$  by this kind of singularities, where  $h$  is the mesh size of grid points.

For nonequilibrium systems, the classical Poisson-Nernst-Planck model [52,53,54] can then be generalized to the Poisson-Nernst-Planck-Fermi model by coupling the flux density equation (in steady state)

$$-\nabla \cdot \mathbf{J}_i(\mathbf{r}) = 0, \mathbf{r} \in \Omega_s \quad (9)$$

of each particle species  $i = 1, \dots, K+1$  (including water) to the PF equation (8), where the flux density is defined as

$$\mathbf{J}_i(\mathbf{r}) = -D_i \left[ \nabla C_i(\mathbf{r}) + \beta_i C_i(\mathbf{r}) \nabla \phi(\mathbf{r}) - C_i(\mathbf{r}) \nabla S^{\text{trc}}(\mathbf{r}) \right] \quad (10)$$

and  $D_i$  is the diffusion coefficient. The flux equation (9) is called the Nernst-Planck-Fermi equation because the Fermi steric potential  $S^{\text{trc}}(\mathbf{r})$  is introduced to the classical NP equation. The NPF equation (9) reduces to the Fermi distribution (5) at equilibrium [43].

The gradient of the steric potential  $\nabla S^{\text{trc}}$  in (10) represents an entropic force of vacancies exerted on particles. The negative sign in  $-C_i \nabla S^{\text{trc}}$  means that the steric force  $\nabla S^{\text{trc}}$  is in the opposite direction to the ‘diffusional’ force  $\nabla C_i$ , i.e., the larger  $S^{\text{trc}} = \ln \frac{\Gamma(\mathbf{r})}{\Gamma_B}$  (meaning more space available to the particle as implied by the numerator) at  $\mathbf{r}$  in comparison with that of neighboring locations, the more the entropic force pushes the particle to the location  $\mathbf{r}$ . The entropic force is simply opposite to the diffusional force  $\nabla C_i$  that pushes the particle away from  $\mathbf{r}$  if the concentration is larger at  $\mathbf{r}$  than that of neighboring locations. Moreover, the Nernst-Einstein relationship [46] implies that the steric flux  $D_i C_i \nabla S^{\text{trc}}$  is greater if the particle is more mobile. Therefore, the gradients of electric and steric potentials ( $\nabla \phi$  and  $\nabla S^{\text{trc}}$ ) describe the charge/space competition mechanism of particles in a crowded region within a mean-field framework [43]. For more physical and mathematical details about the PNP theory, we refer to [43].

### III. A GENERALIZED SCHARFETTER-GUMMEL METHOD

We use the standard 7-point finite difference (FD) scheme in 3D [45] to discretize the PNP model. For ease of notation, we omit the subscript  $i$  in (9) when no confusion should arise. For conciseness, the FD discretization is simplified to 1D in the following discussions as the corresponding 3D case follows obviously in a similar way. Furthermore, we only provide the FD formula for the flux equation (9) as the FD formulas with the SMIB method across the molecular surface  $\partial\Omega_m$  for Eqs. (6) and (7) have been given in [45], i.e., we consider

$$\frac{dJ(x)}{dx} = \frac{d}{dx} \left[ -D(x) \left( \frac{dC(x)}{dx} + \beta C(x) \frac{d\phi(x)}{dx} - C(x) \frac{dS^{\text{trc}}(x)}{dx} \right) \right] = 0. \quad (11)$$

The primitive FD approximation of (11) is

$$\frac{a_{i-1}C_{i-1} + a_i C_i + a_{i+1}C_{i+1}}{\Delta x^2} = 0, \quad (12)$$

where  $\Delta x = x_{i+1} - x_i = h$  is the mesh size of a uniform grid on the  $x$ -axis in the domain,  $C_i \approx C(x_i)$  is the unknown approximation of the concentration



function  $C(x)$  at any grid point  $x_i$ , and the coefficients are given as

$$\begin{cases} a_{i-1} = D_{i-\frac{1}{2}} \left[ 1 - \beta \Delta \phi_{i-1} / 2 + \Delta S_{i-1}^{\text{trc}} / 2 \right] \\ a_i = a_{i-1} + a_{i+1} - 2(D_{i-\frac{1}{2}} + D_{i+\frac{1}{2}}) \\ a_{i+1} = D_{i+\frac{1}{2}} \left[ 1 + \beta \Delta \phi_i / 2 - \Delta S_i^{\text{trc}} / 2 \right], \end{cases} \quad (13)$$

where  $\Delta \phi_{i-1} = \phi_i - \phi_{i-1}$ ,  $\phi_i \approx \phi(x_i)$ ,  $x_{i+\frac{1}{2}} = (x_{i+1} + x_i) / 2$  etc. The diffusion coefficient function  $D(x)$  is equal to a constant  $D^B$  in the bath and to a reduced constant  $\theta D^B$  in the channel pore with  $0 < \theta < 1$ . The function  $D(x)$  along the channel axis is constructed by using the interpolation method presented in [22] for connecting the bath value  $D^B$  and the pore value  $\theta D^B$  such that  $D(x)$  is a continuously differentiable function. The factor  $\theta$  is the only tuning parameter in the PNPf model to fit experimental data [15,22,28,35,36,40,55,56]. We shall investigate the magnitude of  $\theta$  for GA channel and compare it with those obtained by MD and BD simulations. The comparison is used to verify the correlation and steric effects considered in PNPf.

At any two adjacent grid points  $x_i$  and  $x_{i+1}$ , the FD approximation of the zero flux ( $J(x) = 0$ ) is

$$\frac{C_{i+1} - C_i}{\Delta x} = \frac{C_{i+1} + C_i}{2} \left( -\beta \frac{\Delta \phi_i}{\Delta x} + \frac{\Delta S_i^{\text{trc}}}{\Delta x} \right), \quad (14)$$

which implies that we may obtain the inequality

$$C_{i+1} - C_i > C_{i+1} + C_i \quad (15)$$

and thereby a negative (*unphysical*) concentration  $C_i < 0$  at  $x_i$  if

$$\frac{1}{2} \left( -\beta \Delta \phi_i + \Delta S_i^{\text{trc}} \right) > 1. \quad (16)$$

Without the steric term  $\Delta S^{\text{trc}}$ , this inequality is the well-known Scharfetter-Gummel stability condition in semiconductor device simulations [2,7]

$$-\Delta \phi_i = -(\phi_{i+1} - \phi_i) \leq \frac{2}{\beta} = \frac{2k_B T}{q} \quad (\text{for } \beta > 0) \quad (17)$$

required to ensure that the FD equation (12) does not produce unphysical approximations. Note that  $q = 2e$  for  $\text{Ca}^{2+}$  yields an upper bound  $k_B T / e$  in (17), which is a half of that for  $\text{Na}^+$  and means that if the potential difference  $-\Delta \phi_i$  between two adjacent points is greater than  $k_B T / e \approx 25.7$  mV at room temperature, the resulting approximation of the  $\text{Ca}^{2+}$  flux  $\mathbf{J}_{\text{Ca}^{2+}}$  in (9) may be completely unphysical, although the same discretization of the  $\text{Na}^+$  flux  $\mathbf{J}_{\text{Na}^+}$  may still be feasible. In other words, the FD formula (12) is more unstable

for  $\text{Ca}^{2+}$  than for  $\text{Na}^+$ . In fact, if the SG condition is violated, Newton's iteration for solving the coupled PNP system of nonlinear algebraic equations is generally divergent. Of course, we could reduce the mesh size  $\Delta x$  so that the difference  $-\Delta\phi_i$  is small enough to satisfy (17) at all grid points  $i$ . This would however incur larger algebraic systems (and thus larger conditioning numbers of the system) for which the computational cost would be more expensive. Even using adaptive meshes that efficiently resolve internal or boundary layer regions where  $-\Delta\phi_i$  varies sharply, the primitive approximation (12) would still diverge or show extremely slow convergence if the layer thickness is very small [16,18,19].

The convergence and stability issues are further complicated by the steric potential  $S^{\text{trc}}$  in ion channel simulations if it is added to the FD flux equation (12) as given in (13). From (16), we obtain a new SG condition for ion channels

$$-\beta\Delta\phi_i + \Delta S_i^{\text{trc}} \leq 2 \quad (18)$$

that will be a focal point in our numerical investigations in Section 5.

**Stabilization.** To stabilize (12), we extend the classical Scharfetter-Gummel approximation [2] of the flux  $J(x)$  to include the steric potential such that

$$J_{i+\frac{1}{2}} = -\frac{D}{\Delta x} [B(-t_i)C_{i+1} - B(t_i)C_i] \quad (19)$$

where  $t_i = \beta\Delta\phi_i - \Delta S_i^{\text{trc}}$  and  $B(t) = \frac{t}{e^t - 1}$  is the Bernoulli function [7]. Eq. (19) is an exponential fitting scheme for the concentration function  $C(x)$  between the mesh points  $x_i$  and  $x_{i+1}$  and is derived from the assumption that the flux  $J$ , the local electric field  $\frac{-d\phi}{dx}$ , and the local steric field  $\frac{dS^{\text{trc}}}{dx}$  are all constant in this subinterval, i.e.,

$$\frac{J}{D} = \frac{-dC(x)}{dx} - kC(x), \text{ for all } x \in (x_i, x_{i+1}), \quad (20)$$

where  $k = \beta\frac{d\phi}{dx} - \frac{dS^{\text{trc}}}{dx}$ . Solving this ordinary differential equation (ODE) with a boundary condition  $C_i$  or  $C_{i+1}$  yields the well-known Goldman-Hodgkin-Katz flux equation in ion channels [46], which is exactly the same as that in (19).

The generalized Scharfetter-Gummel method for (11) is thus

$$\begin{aligned}
\frac{dJ(x_i)}{dx} &\approx \frac{J_{i+\frac{1}{2}} - J_{i-\frac{1}{2}}}{\Delta x} = \frac{a_{i-1}C_{i-1} + a_iC_i + a_{i+1}C_{i+1}}{\Delta x^2} = 0 \\
J_{i-\frac{1}{2}} &= \frac{-D}{\Delta x} [B(-t_{i-1})C_i - B(t_{i-1})C_{i-1}] \\
J_{i+\frac{1}{2}} &= \frac{-D}{\Delta x} [B(-t_i)C_{i+1} - B(t_i)C_i] \\
t_i &= \beta\Delta\phi_i - \Delta S_i^{\text{trc}}, \quad B(t) = \frac{t}{e^t - 1} \\
a_{i-1} &= -B(t_{i-1}), \quad a_i = B(-t_{i-1}) + B(t_i), \quad a_{i+1} = -B(-t_i).
\end{aligned} \tag{21}$$

The SG method is *optimal* in the sense that it integrates the ODE (20) *exactly* at *every* grid point with a suitable boundary condition [5]. Therefore, the SG method can resolve sharp layers very accurately [5] and hence needs few grid points to obtain tolerable approximations when compared with the primitive FD method. Moreover, the exact solution of (20) for the concentration function  $C(x)$  yields an exact flux  $J(x)$ . Consequently, the SG method is current-preserving, which is particularly important in nonequilibrium systems, where the current is possibly the most relevant physical property of interest [10]. It is difficult to overstate the importance of the current preserving feature and it must be emphasized for workers coming from fluid mechanics that preserving current has a significance quite beyond the preserving of flux in uncharged systems. The electric field is so strong that the tiniest error in preserving current, i.e., the tiniest deviation from Maxwell's equations, produces huge effects. The third paragraph of Feynman's lectures on electrodynamics makes this point unforgettable [57]. Thus, the consequences of a seemingly small error in preserving the flow of charge are dramatically larger than the consequences of the same error in preserving the flux of mass.

#### IV. SMIB-SG AND MULTISCALE METHODS

To test the PNPF theory and verify the numerical methods developed in this paper, we consider the GA channel with a real protein structure and a simplified molecular model of L-type calcium channels. The main difference between these two channels is that the GA channel has a more rigid and less negatively charged pore with about 2 Å in radius whereas the  $\text{Ca}^{2+}$  channel has a flexible and higher negatively charged binding site with radius varying from 1 Å to 2.5 Å. The GA channel is also much longer (22 Å, see below) than the selectivity filter of the L type calcium channel (10 Å [58]). Consequently, the GA channel is only cation selective whereas the  $\text{Ca}^{2+}$  channel is exquisitely  $\text{Ca}^{2+}$  selective. The steric potential is a key component of PNPF to properly describe this important difference in selectivity along with the size effect of

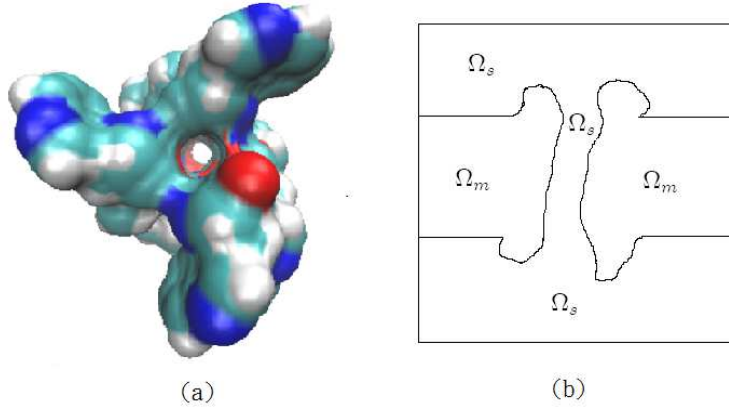


Fig. 1. (Color online.) (a) Top view of the gramicidin A channel. (b) A cross section of 3D simulation domain for the GA channel. The channel is placed in a cubic box with the length of each side being 40 Å and the thickness of the membrane being 24 Å.

water (1.4 Å in radius). We use two different treatments of water that yield two different steric potentials and size effects.

### A. The SMIB-SG Method for Gramicidin A Channel

Fig. 1(a) is a top view of the GA channel downloaded from the Protein Data Bank [59]. A 2D cross section of the 3D simulation domain of the channel embedded in a membrane is sketched in Fig. 1(b), where the biomolecular domain  $\Omega_m$  is composed of the channel protein and the membrane and the solvent domain  $\Omega_s$  consists of extracellular (upper), channel pore (central), and intracellular (lower) regions. Particle species are indexed by 1, 2, and 3, for  $K^+$ ,  $Cl^-$ , and  $H_2O$  with radii  $a_1 = a_{K^+}$ ,  $a_2 = a_{Cl^-}$ , and  $a_3 = a_{H_2O}$  given in Table I.

The SMIB method is an advanced method to treat singularities of protein charges and molecular surfaces [22,44,45]. In SMIB, the electric potential generated by the protein charges ( $q_j\delta(\mathbf{r} - \mathbf{r}_j)$  in (8)) is modeled as a sum of an analytical Green function  $\phi^*$  in infinite space and the Laplace potential  $\phi^0$  in the biomolecular domain  $\Omega_m$  with boundary values of  $\phi^*$  on  $\partial\Omega_m$ . The combined potential then defines an electric field  $-\nabla(\phi^* + \phi^0)$  that acts on ions and water in the solvent domain  $\Omega_s$  from the molecular surface  $\partial\Omega_m$ . The total potential  $\phi$  of all charged objects (ions, atomic charges, and polarized water) is then calculated by solving Eqs. (6) and (7) with the SMIB method for Eq. (7) across the interface  $\partial\Omega_m$  of dielectric solvent  $\Omega_s$  and molecular  $\Omega_m$  domains.

TABLE I. Notations and Physical Constants

Symbol	Meaning	Value	Unit
$k_B$	Boltzmann constant	$1.38 \times 10^{-23}$	J/K
$T$	temperature	298.15	K
$e$	proton charge	$1.602 \times 10^{-19}$	C
$\epsilon_0$	permittivity of vacuum	$8.85 \times 10^{-14}$	F/cm
$\epsilon_w$	water dielectric constant	80 or 78.5	
$\epsilon_m$	protein dielectric constant	2	
$\hat{\epsilon} = \epsilon_s(1 - l_c^2 \nabla^2)$	dielectric operator, $\epsilon_s = \epsilon_w \epsilon_0$	in Eq. (6)	F/cm
$\tilde{\epsilon}(\mathbf{r}) \approx \hat{\epsilon}$	dielectric function	in Eqs. (6), (31)	
$a_{\text{Na}^+}, a_{\text{Ca}^{2+}}$	particle radii	0.95, 0.99	Å
$a_{\text{K}^+}, a_{\text{Cl}^-}, a_{\text{H}_2\text{O}}$	particle radii	1.33, 1.81, 1.4	Å
$l_c$	correlation length	$1.2a_{\text{K}^+}$ or $2a_{\text{Ca}^{2+}}$	Å
$D_{\text{K}^+}^B$	$\text{K}^+$ diffusion coefficient	$1.96 \times 10^{-5}$	$\text{cm}^2/\text{s}$
$D_{\text{Na}^+}^B$	$\text{Na}^+$ diffusion coefficient	$1.334 \times 10^{-5}$	$\text{cm}^2/\text{s}$
$D_{\text{Ca}^{2+}}^B$	$\text{Ca}^{2+}$ diffusion coefficient	$0.792 \times 10^{-5}$	$\text{cm}^2/\text{s}$
$D_{\text{Cl}^-}^B$	$\text{Cl}^-$ diffusion coefficient	$2.032 \times 10^{-5}$	$\text{cm}^2/\text{s}$
$D_{\text{H}_2\text{O}}^B$	$\text{H}_2\text{O}$ diffusion coefficient	$2.3 \times 10^{-5}$	$\text{cm}^2/\text{s}$
$V_{i,o}$	inside (outside) voltage		V

The molecular surface  $\partial\Omega_m$  as depicted in Fig. 1(a) is generated by rolling a probe ball (water molecule) with radius 1.4 Å over a total of 554 spherical atoms in the GA protein [60]. In SMIB, the molecular surface is not fixed and is adaptively determined by the grid size so that the interface point is always in the middle of neighboring grid points. The resulting surface is thus free of geometric singularities. We refer to [45] for more details about the SMIB and surface generation methods.

The NP equation (9) is then solved by the SG method for each particle species  $i$  once  $\phi$  is known. An iterative process of solving PF1 (6), PF2 (7), and NP equations is repeated again until convergent approximations of  $\phi(\mathbf{r})$  and  $C_i(\mathbf{r})$  are found at all grid points. As noted above, convergence of this kind of iterative process is in general not guaranteed and must be checked at all grid points. We propose the following nonlinear iteration algorithm for the PNP system (6), (7), and (9) using SMIB and SG methods:

*Nonlinear Iteration Algorithm 1:*

1. Solve the Laplace equation  $-\nabla^2 \phi^0(\mathbf{r}) = 0$  in  $\Omega_m$  for the potential  $\phi^0(\mathbf{r})$  once for all with  $\phi^0(\mathbf{r}) = \phi^*(\mathbf{r}) = \sum_{j=1}^Q q_j / (4\pi\epsilon_m\epsilon_0 |\mathbf{r} - \mathbf{r}_j|)$  on  $\partial\Omega_m$ .
2. Solve the Poisson equation  $-\nabla \cdot (\epsilon \nabla \phi(\mathbf{r})) = 0$  in  $\Omega$  at equilibrium for the initial potential  $\phi^{\text{Old}}(\mathbf{r})$  with  $\phi^{\text{Old}} = 0$  on  $\partial\Omega$  and the jump condition  $[\epsilon \nabla \phi^{\text{Old}} \cdot \mathbf{n}] = -\epsilon_m\epsilon_0 \nabla(\phi^* + \phi^0) \cdot \mathbf{n}$  on  $\partial\Omega_m$ , where  $[u]$  denotes the jump function across  $\partial\Omega_m$  [45].
3. Solve the PF1  $\epsilon_s (l_c^2 \nabla^2 - 1) \Psi(\mathbf{r}) = \sum_{i=1}^K q_i C_i^{\text{Old}}(\mathbf{r})$  in  $\Omega_s$  for  $\Psi^{\text{New}}(\mathbf{r})$  with  $\nabla \Psi^{\text{New}} \cdot \mathbf{n} = 0$  on  $\partial\Omega_m$ ,  $\Psi^{\text{New}} = 0$  on  $\partial\Omega$ , and the Fermi distribution  $C_i^{\text{Old}}(\mathbf{r}) = C_i^{\text{B}} \exp(-\beta_i \phi^{\text{Old}}(\mathbf{r}) + S^{\text{trc}}(\mathbf{r}))$ ,  $S^{\text{trc}}(\mathbf{r}) = \ln \frac{\Gamma^{\text{Old}}(\mathbf{r})}{\Gamma^{\text{B}}}$ ,  $\Gamma(\mathbf{r}) = 1 - \sum_{j=1}^{K+1} v_j C_j^{\text{Old}}(\mathbf{r})$ .
4. Solve the linearized PF2  $-\nabla \cdot (\epsilon \nabla \phi(\mathbf{r})) + \rho'(\phi^{\text{Old}}) \phi(\mathbf{r}) = -\epsilon \Psi^{\text{New}} + \rho'(\phi^{\text{Old}}) \phi^{\text{Old}}$  at equilibrium for the next potential  $\phi^{\text{New}}(\mathbf{r})$  with the same jump and boundary conditions in Step 2. Here  $\rho'(\phi)$  denotes the derivative of the charge density functional  $\rho(\phi) = \sum_{i=1}^K q_i C_i^{\text{B}} \exp(-\beta_i \phi + S^{\text{trc}})$  in  $\Omega_s$  with respect to  $\phi$ .
5. Assign  $\phi^{\text{Old}} = \omega_{\text{PF}} \phi^{\text{Old}} + (1 - \omega_{\text{PF}}) \phi^{\text{New}}$  with a suitable relaxation parameter  $\omega_{\text{PF}}$  and go to Step 3 if the error  $\|\phi^{\text{New}} - \phi^{\text{Old}}\|_{\infty}$  in the infinity norm is larger than a preset tolerance, else go to Step 6.
6. Solve the steady state NP equation  $-\nabla \cdot \mathbf{J}_i(\mathbf{r}) = 0$  in  $\Omega_s$  at nonequilibrium for  $C_i^{\text{New}}(\mathbf{r})$  and all  $i = 1, \dots, K+1$  with  $\mathbf{J}_i(\mathbf{r}) = -D_i [\nabla C_i(\mathbf{r}) + \beta_i C_i(\mathbf{r}) \nabla \phi^{\text{Old}}(\mathbf{r}) - C_i(\mathbf{r}) \nabla S^{\text{trc}}(\mathbf{r})]$ ,  $S^{\text{trc}}(\mathbf{r}) = \ln \frac{\Gamma^{\text{Old}}(\mathbf{r})}{\Gamma^{\text{B}}}$ ,  $C_i^{\text{New}}(\mathbf{r}) = 0$  on  $\partial\Omega$ , and  $\mathbf{J}_i(\mathbf{r}) \cdot \mathbf{n} = 0$  on  $\partial\Omega_m$ .
7. Solve the PF1 for  $\Psi^{\text{New}}$  as in Step 3 with  $C_i^{\text{New}}$  in place of  $C_i^{\text{Old}}$ .
8. Solve the PF2  $-\nabla \cdot (\epsilon \nabla \phi(\mathbf{r})) = -\epsilon \Psi^{\text{New}}$  (without linearization) at nonequilibrium for  $\phi^{\text{New}}$ .
9. Assign  $\phi^{\text{Old}} = \omega_{\text{PNPF}} \phi^{\text{Old}} + (1 - \omega_{\text{PNPF}}) \phi^{\text{New}}$  with a suitable relaxation parameter  $\omega_{\text{PNPF}}$  and go to Step 6 if  $\|\phi^{\text{New}} - \phi^{\text{Old}}\|_{\infty}$  is larger than a preset error tolerance, else stop.

This is an SOR-like iteration algorithm modified from that in [22]. The modifications include the additional solution processes at equilibrium in Steps 2, 3, and 4, the extra PF1 in Steps 3 and 7, Newton's linearization for PF2 in Step 4, two relaxation parameters  $\omega_{\text{PF}}$  and  $\omega_{\text{PNPF}}$  in Step 5 and 9 with  $0 < \omega_{\text{PF}}, \omega_{\text{PNPF}} < 1$  (under relaxation), and the extra water NP equation  $-\nabla \cdot \mathbf{J}_{K+1}(\mathbf{r}) = 0$  in Step 6. The stability and convergence rate are controlled by these two parameters. If the parameter is close to zero, we will have more stable iteration but slower convergence. The correlation length  $l_c$  and the Fermi distribution (or the steric potential  $S^{\text{trc}}$ ) in Step 3 signify the difference between the classical PNP and advanced PNPF models. The stability and convergence are further complicated by these two physical properties for which a continuation method may be needed by introducing two stepping parameters  $\lambda_c$  and  $\lambda_S$  such that  $\lambda_c l_c$  and  $\lambda_S S^{\text{trc}}$  are gradually increased from  $\lambda_c = \lambda_S = 0$  to  $\lambda_c = \lambda_S = 1$  [45].

The water NP equation is not considered in previous PNP models and plays an essential role not only for numerical stability but also for physical validity because the void volume fraction  $\Gamma(\mathbf{r}) = 1 - \sum_{j=1}^{K+1} v_j C_j(\mathbf{r})$  in Step 3 at any location  $\mathbf{r}$  in the solvent domain  $\Omega_s$  needs to be carefully checked in each iteration. Numerical errors in approximating the concentration functions  $C_j(\mathbf{r})$  for any particle species  $j = 1, \dots, K + 1$  could easily lead to an unphysical void fraction  $\Gamma(\mathbf{r}) < 0$  at some  $\mathbf{r}$ . Water molecules automatically adjust themselves in the PNPF model and move together with all ions in the system as the above iteration process converges to a stable and correct state, although the net water flow through the channel may be zero. Moreover, the water NP equation also dynamically determines the variable permittivity  $\tilde{\epsilon}(\mathbf{r})\epsilon_0 = \epsilon_s/(1 + \eta(\mathbf{r})/\rho(\mathbf{r}))$  from the bath to the pore and thus automatically adjusts dielectric forces on ions along the channel pathway. These dielectric forces can have a decisive effect on biologically important conductance [61] and on selectivity. For example,  $\text{Na}^+$  vs.  $\text{K}^+$  selectivity in  $\text{Na}^+$  channels is only found when the dielectric function is handled in more detail [62,63].

However, this SMIB-SG method and previous PNP methods suffer from a major difficulty in ion channel simulations. Those methods have difficulty in dealing with the essential property of selectivity, which of course is different in different types of channels with different structures. The L-type calcium channel selects  $\text{Ca}^{2+}$  over  $\text{Na}^+$  of similar size and a potassium channel selects  $\text{K}^+$  over  $\text{Na}^+$  of the same charge. The following method is proposed to overcome this difficulty.

## B. A Multiscale Method for Calcium Channel

Calcium channels have not yet been crystallized and so we use the Lipkind-Fozzard molecular model [64] of L-type calcium channels in which the EEEE locus (four glutamate side chains modeled by 8  $\text{O}^{1/2-}$  ions) forms a high-affinity  $\text{Ca}^{2+}$  binding site that is essential to  $\text{Ca}^{2+}$  selectivity, blockage, and permeation. Fig. 2(a) illustrates the binding site and the EEEE locus, where 3  $\text{Ca}^{2+}$  are shown in violet, 8  $\text{O}^{1/2-}$  in red, 2  $\text{H}_2\text{O}$  in white and red. Fig. 2(b) is a cross section of a simplified 3D channel geometry for the present work, where the central circle denotes the binding site, the other four circles denote the side view of 8  $\text{O}^{1/2-}$  ions,  $\Omega_s$  is the solvent domain consisting of two baths and the channel pore including the binding domain  $\overline{\Omega}_{\text{Bind}}$ ,  $\Omega_m$  is the biomolecular domain with the boundary  $\partial\Omega_m$ , and  $\partial\Omega$  is the outside and inside bath boundary. Fig. 3 is a sketch of the binding site and  $\text{O}^{1/2-}$  ions, where  $d_O^{Ca}$  is the distance between the center of a binding  $\text{Ca}^{2+}$  ion and the center  $c_j$  of any  $\text{O}^{1/2-}$ , and  $A$  is any point on the surface of the site. In our model, the 8  $\text{O}^{1/2-}$  ions are not contained in the solvent domain  $\Omega_s$ . Particle species are indexed by 1, 2, 3, and 4 for  $\text{Na}^+$ ,  $\text{Ca}^{2+}$ ,  $\text{Cl}^-$ , and  $\text{H}_2\text{O}$ , respectively.

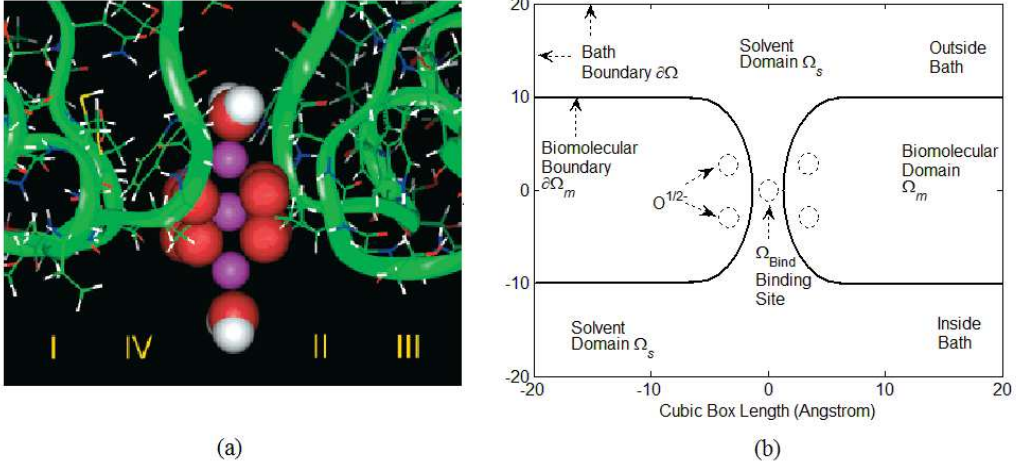


Fig. 2. (Color online.) (a) The Lipkind-Fozzard pore model, where 3  $\text{Ca}^{2+}$  are shown in violet, 8  $\text{O}^{1/2-}$  in red, 2  $\text{H}_2\text{O}$  in white and red. Reprinted with permission from (G. M. Lipkind and H. A. Fozzard, *Biochem.* **40**, 6786 (2001)). Copyright (2001) American Chemical Society. (b) A simplified Ca channel geometry in a cubic box with baths, pore, and binding site. The solvent region  $\Omega_s$  consists of two baths and the channel pore. The binding site  $\bar{\Omega}_{\text{Bind}}$  is contained in  $\Omega_s$  but the  $\text{O}^{1/2-}$  ions are not in  $\Omega_s$ . The outside and inside bath boundary is denoted by  $\partial\Omega$ .

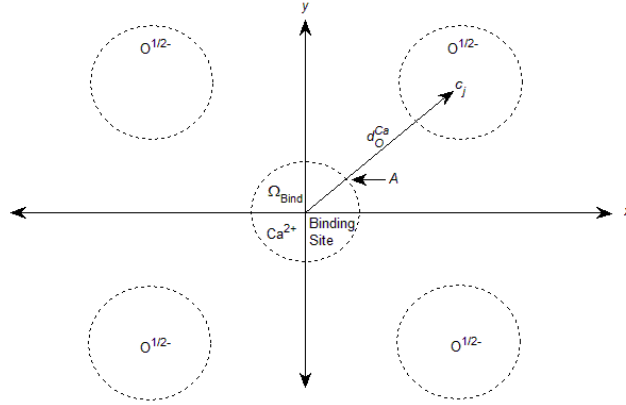


Fig. 3. The binding distance between the center of the binding  $\text{Ca}^{2+}$  ion and the center  $c_j$  of the  $j^{\text{th}}$   $\text{O}^{1/2-}$  ion is denoted by  $d_{\text{O}}^{\text{Ca}}$  for  $j = 1, \dots, 8$ .  $A$  is any point on the surface of the binding ion.

In [65], we proposed an algebraic model for calculating the electrical potential  $\bar{\phi}_b$  and the steric potential  $\bar{S}_b^{\text{trc}}$  in  $\bar{\Omega}_{\text{Bind}}$  by using Coulomb's law with the atomic structure of binding ion and atoms in a channel protein as shown in Fig. 3, without solving the Poisson-Fermi equation (8) in  $\bar{\Omega}_{\text{Bind}}$ . The volume of  $\bar{\Omega}_{\text{Bind}}$  is an unknown variable  $v_b$  that changes with different charges in the binding site. The algebraic model [65] defined in  $\bar{\Omega}_{\text{Bind}}$  consists of the following



equations

$$\begin{cases} O_1^b = v_b C_1^B \exp(-\beta_1 \bar{\phi}_b + \bar{S}_b^{\text{trc}}) \\ O_2^b = v_b C_2^B \exp(-\beta_2 \bar{\phi}_b + \bar{S}_b^{\text{trc}}) \\ O_4^b = v_b C_4^B \exp(\bar{S}_b^{\text{trc}}), \end{cases} \quad (22)$$

$$\bar{S}_b^{\text{trc}} = \ln \frac{v_b - v_1 O_1^b - v_2 O_2^b - v_4 O_4^b}{v_b \Gamma^B}, \quad (23)$$

$$\frac{e}{4\pi\epsilon_0} \left( \sum_{j=1}^8 \frac{z_{\text{O}^{1/2-}}}{|c_j - A|} + \frac{O_1^b z_{\text{Na}^+}}{a_{\text{Na}^+}} + \frac{O_2^b z_{\text{Ca}^{2+}}}{a_{\text{Ca}^{2+}}} \right) = \bar{\phi}_b, \quad (24)$$

where  $O_1^b$ ,  $O_2^b$ , and  $O_4^b$  denote the occupancy numbers of  $\text{Na}^+$ ,  $\text{Ca}^{2+}$ , and  $\text{H}_2\text{O}$  in  $v_b$ , respectively,  $\bar{\phi}_b$  and  $\bar{S}_b^{\text{trc}}$  are average electrical and steric potentials, and  $|c_j - A|$  is the distance between  $A$  and  $c_j$  in Fig. 3.

In this mean field, we allow  $O_1^b$  and  $O_2^b$  (and hence the total charge  $O_1^b e z_{\text{Na}^+} + O_2^b e z_{\text{Ca}^{2+}}$ ) to vary continuously subject to the condition on their sum  $O_1^b + O_2^b = 1$  in the binding volume  $v_b$ . Eqs. (22) and (23) uniquely determine the four unknowns  $v_b$ ,  $O_4^b$ ,  $\bar{\phi}_b$  and  $\bar{S}_b^{\text{trc}}$  with  $O_1^b$  and  $O_2^b$  being given. Eq. (24) uniquely determines the locations ( $c_j$ ) of 8  $\text{O}^{1/2-}$  ions (and thus the binding distance  $d_O^{Ca}$  or  $d_O^{Na}$  in Fig. 3) once  $\bar{\phi}_b$  is obtained. Note that the binding distance  $d_O^{O_1^b \text{Na} + O_2^b \text{Ca}}$  (or  $c_j$ ) changes continuously with varying  $O_1^b$  and  $O_2^b$  but  $\bar{\phi}_b$  remains fixed, where the binding ion  $O_1^b \text{Na} + O_2^b \text{Ca}$  is a linear combination of  $\text{Na}^+$  and  $\text{Ca}^{2+}$ . Therefore,  $\text{O}^{1/2-}$  ions are movable — the protein is flexible in our model — as their locations  $c_j$  changes with varying  $O_1^b$  and  $O_2^b$ .

For the half-blockage experimental condition [66]

$$\underbrace{C_{\text{Na}^+}^B = C_1^B = 32 \text{ mM}, C_{\text{Ca}^{2+}}^B = C_2^B = 0.9 \text{ } \mu\text{M}}_{\text{Experimental Data}}, \quad (25)$$

we follow convention and assume relative occupancies of a filled channel,  $O_1^b = 0.5$  and  $O_2^b = 0.5$ , and thereby obtain  $\bar{\phi}_b = -10.48 \text{ } k_B T / e$ ,  $\bar{S}_b^{\text{trc}} = -1.83$ , and  $v_b = 4.56 \text{ } \text{\AA}^3$  [65]. The binding experiments [66] used a fixed  $C_{\text{Na}^+}^B = C_1^B = 32 \text{ mM}$  and various  $\text{Ca}^{2+}$  bath concentrations  $C_{\text{Ca}^{2+}}^B = C_2^B$  that imply different  $O_1^b$  and  $O_2^b$  of  $\text{Na}^+$  and  $\text{Ca}^{2+}$  occupying the binding site. The occupancy numbers  $O_1^b$  and  $O_2^b$  are determined by

$$\frac{O_1^b}{O_2^b} = \frac{1 - O_2^b}{O_2^b} = \exp(-(\beta_1 - \beta_2) \bar{\phi}_b) \frac{C_1^B}{C_2^B}, \quad (26)$$

where  $\bar{\phi}_b$  was just obtained from the case of equal occupancy. The occupancy ratio in (26) thus deviates from unity as  $C_2^B$  is varied along the horizontal axis of the binding curve from its midpoint value  $C_2^B = 0.9 \text{ } \mu\text{M}$  as shown in Fig. 5 in [65].

For nonequilibrium cases, the binding steric potential  $\bar{S}_b^{\text{trc}}$  is assigned its equilibrium value in subsequent PNPF calculations, i.e., the void fraction  $\Gamma(\mathbf{r})$  in  $\bar{\Omega}_{\text{Bind}}$  is assumed to remain unchanged from equilibrium to nonequilibrium. The electrical potential  $\bar{\phi}_b$  will be modified by the membrane potential  $V_i - V_o$  [14] and then used as a Dirichlet type condition for the potential function  $\phi(\mathbf{r})$  in  $\bar{\Omega}_{\text{Bind}}$ . For this multiscale method, the boundary conditions for the PF (8) and NP (9) equations are

$$\begin{cases} \phi(\mathbf{r}) = \tilde{\phi}_b(\mathbf{r}) \text{ in } \bar{\Omega}_{\text{Bind}}, \phi(\mathbf{r}) = V_{o,i} \text{ on } \partial\Omega, \\ C_i(\mathbf{r}) = C_i^{\text{B}} \text{ on } \partial\Omega, i = 1, 2, 3, 4, \\ \mathbf{J}_i(\mathbf{r}) \cdot \mathbf{n} = 0 \text{ on } \partial\Omega_m. \end{cases} \quad (27)$$

Note that the electrostatic potential  $\phi(\mathbf{r})$  is prescribed as a Dirichlet function  $\tilde{\phi}_b(\mathbf{r})$  whose spatial average in  $\bar{\Omega}_{\text{Bind}}$  is the constant  $\bar{\phi}_b$ . However, the binding domain  $\bar{\Omega}_{\text{Bind}}$  is treated as an interior domain instead of boundary domain for the NP equation (9).

If a condition on the boundary is used to solve the Poisson (or PF) equation as in Algorithm 1, the resulting steric potential  $\bar{S}_b^{\text{trc}}$  (as an output of  $\phi(\mathbf{r})$  by (5)) may be incorrect in  $\bar{\Omega}_{\text{Bind}}$  because the atomic equations (23) and (24) are not used. We do not have any differential equation for the steric function  $S^{\text{trc}}(\mathbf{r})$  for which appropriate boundary conditions near  $\bar{\Omega}_{\text{Bind}}$  can be imposed if a conventional method is used. The methods proposed in this paper are still coarse approximations to ion transport as the PNPF theory is in its early development. Nevertheless, the theory provides many atomic properties such as (23) and (24) that have been shown to be important for studying the binding mechanism in Cav channels [65] and are also important for the transport mechanism as shown in the next section. Incorporating atomic properties into continuum models is a step forward to improve and refine the continuum theory. We refer to [43,65] for more details of the algebraic model and its extension to PNPF.

We summarize the PNPF solution process using the multiscale method as follows.

*Nonlinear Iteration Algorithm 2:*

1. Solve (23) and (24) for  $\bar{\phi}_b$  and  $\bar{S}_b^{\text{trc}}$  in the binding site  $\bar{\Omega}_{\text{Bind}}$  with the experimental data (25).
2. Choose any linear interpolation  $\bar{\phi}^{\text{Old}}$  (an initial guess potential profile) that links the binding potential  $\phi_A$  to the zero potential at each bath boundary for the potential function  $\phi(\mathbf{r})$ .
3. Solve the PB equation  $-\nabla \cdot (\epsilon \nabla \phi(\mathbf{r})) = \rho(\bar{\phi}^{\text{Old}}) = \sum_{i=1}^K q_i \bar{C}_i^{\text{Old}}$  at equilib-

rium for  $\phi^{\text{Old}}$  with the Boltzmann distribution  $\bar{C}_i^{\text{Old}} = C_i^{\text{B}} \exp(-\beta_i \bar{\phi}^{\text{Old}})$ .

Compute the initial concentrations  $C_i^{\text{Old}} = C_i^{\text{B}} \exp(-\beta_i \phi^{\text{Old}})$ .

4. Solve the PF1  $\epsilon_s (l_c^2 \nabla^2 - 1) \Psi(\mathbf{r}) = \sum_{i=1}^K q_i C_i^{\text{Old}}(\mathbf{r})$  in  $\Omega_s$  for  $\Psi^{\text{New}}(\mathbf{r})$  with the same conditions as in Algorithm 1.
5. Solve the linearized PF2  $-\nabla \cdot (\epsilon \nabla \phi(\mathbf{r})) + \rho'(\phi^{\text{Old}}) \phi(\mathbf{r}) = -\epsilon \Psi^{\text{New}} + \rho'(\phi^{\text{Old}}) \phi^{\text{Old}}$  in  $\Omega_s$  at nonequilibrium for  $\phi^{\text{New}}$  with the conditions in (27).
6. Solve the NP equation  $-\nabla \cdot \mathbf{J}_i(\mathbf{r}) = 0$  in  $\Omega_s$  at nonequilibrium for  $C_i^{\text{New}}(\mathbf{r})$  and all  $i = 1, \dots, K+1$  with the same conditions as in Algorithm 1.
7. Go to Step 4 if  $\|\phi^{\text{New}} - \phi^{\text{Old}}\|_{\infty}$  or  $\|C_i^{\text{New}} - C_i^{\text{Old}}\|_{\infty}$  is larger than a preset error tolerance, else stop.

We do not need to solve the Poisson equation in the biomolecular domain  $\Omega_m$  that contains the singular charges of  $8 \text{ O}^{1/2-}$ , since the effect of these charges on potentials has been included in the integral constraint we apply to the binding potential  $\bar{\phi}_b$  in (24). Consequently, we do not have to deal with the delta function in (8) and the potential jump conditions on  $\partial\Omega_m$  as used in Algorithm 1. The absence of jump conditions makes the approximation of PF1 and PF2 more accurate since numerical methods for handling the jump conditions across molecular surfaces with singular cusps are subtle, complex, and thus prone to error [44,45]. Moreover, the SOR-like scheme is not needed for this iteration. Application of the multiscale method to the NCX structure [67] is briefly discussed in [65]. It will be interesting to apply the method to the celebrated KcsA potassium channel [68] and to recent structures of TRPV1 [69] and Ca<sub>v</sub>Ab channels [70].

## V. NUMERICAL RESULTS

The main purpose of this work is to present numerical methods that are suitable for continuum simulations of ion transport in different types of biological ion channels with particular interests in treating the excluded volume effect of all particles and the dynamical effect of water molecules. Numerical methods are validated for accuracy with exact solutions of the PNP model for the GA channel. Numerical results of the PNP model for both GA and calcium channels are all verified with experimental data.

### A. Gramicidin A Channel

The Scharfetter-Gummel method (21) is first validated with the following exact solutions for the PNP model [22]

$$\phi(\mathbf{r}) = \begin{cases} \cos x \cos y \cos z, & \mathbf{r} = (x, y, z) \in \Omega_m, \\ \cos x \cos y \cos z, & \mathbf{r} \in \Omega_s, \end{cases} \quad (28)$$

$$C_1(\mathbf{r}) = \begin{cases} 0 & \text{in } \Omega_m, \\ 0.2 \cos x \cos y \cos z + 0.3 & \text{in } \Omega_s, \end{cases} \quad (29)$$

$$C_2(\mathbf{r}) = \begin{cases} 0 & \text{in } \Omega_m, \\ 0.1 \cos x \cos y \cos z + 0.3 & \text{in } \Omega_s. \end{cases} \quad (30)$$

Note that the right hand side of the Poisson equation in Algorithm 1 is not zero as the exact solution (28) has been imposed and the Green function  $\phi^*(\mathbf{r}) = \sum_{j=1}^Q q_j / (4\pi\epsilon_m |\mathbf{r} - \mathbf{r}_j|)$  is only used in the jump condition on the molecular surface  $\partial\Omega_m$ , where the coordinates  $\mathbf{r}_j$  of the atoms in the GA channel protein are provided in the Protein Data Bank [59], the protein charge  $q_j$  and the radius of each atom  $j$  are obtained by the PDB2PQR software [71], and the total number of atoms is  $Q = 554$ . The optimal convergence (second) order, i.e.  $O(h^2)$ , of the SMIB method for the nonlinear Poisson-Boltzmann equation has been confirmed in [45]. The need for such validation has been pointed out before [72]. It is easy to mistake convergence for accuracy in systems of PNP like equations [13].

For a full nonlinear PNP system (without steric, correlation, and water NP effects) using Algorithm 1, Table II shows that the optimal convergence order has been achieved for all PNP equations as well by using the SMIB method for the Poisson equation and the primitive FD method (12) for the NP equations in the nonlinear iteration process. In the table, errors are measured in the  $L_\infty$  norm. For example,  $0.0927 = \max_{ijk} |\phi(x_i, y_j, z_k) - \phi_{ijk}|$ , where  $\phi_{ijk}$  is the FD approximation of the Poisson equation and  $\phi(x_i, y_j, z_k)$  is the exact value evaluated by (28) at the grid point  $(x_i, y_j, z_k)$  with the mesh size  $h = 1 \text{ \AA}$ . The error tolerance for both linear solver and nonlinear iteration was set to  $10^{-6}$ . All errors and orders (Ord) of convergence in Table II are similar to those in [22], showing that the SMIB method in [45] is comparable to the original MIB [22].

When the primitive FD method is replaced by the SG method (21) for NP equations, it is surprising that the preset error tolerance  $10^{-6}$  was satisfied by all SG approximations  $\phi_{ijk}$ ,  $C_1^{ijk}$ , and  $C_2^{ijk}$  at all grid points for all mesh sizes as shown in Table III. Errors in Table III are much more smaller than those in Table II. This demonstrates that the SG is an optimal (exponential fitting) method to discretize the NP equation as implied by the exact analysis of the ODE (20), since all solution functions in (28)-(30) are very smooth so that the assumptions made in (20) are valid. It only took 2 nonlinear iterations and about 1 hour and 8 minutes on a laptop computer with 2.6 GHz Intel CPU to reach the error tolerance for the case of  $h = 0.25 \text{ \AA}$ . The corresponding matrix size is about 4.2 millions. The maximum potential difference  $\Delta\phi_i$  between any two adjacent grid points for the most coarse case ( $h = 1 \text{ \AA}$ ) is -1.045 (not shown), which satisfies the SG condition (18). This illustrates why the convergence has been achieved by the primitive FD without SG as shown in

Table II.

TABLE II. Errors in $L_\infty$ norm by FD							TABLE III. Errors by SG		
$h$ (Å)	P	Ord	NP1	Ord	NP2	Ord	P	NP1	NP2
1.00	0.0927		0.0505		0.0211		$10^{-6}$	$10^{-6}$	$10^{-6}$
0.50	0.0245	1.91	0.0076	2.73	0.0042	2.33	$10^{-6}$	$10^{-6}$	$10^{-6}$
0.25	0.0060	2.03	0.0019	2.00	0.0010	2.07	$10^{-6}$	$10^{-6}$	$10^{-6}$

We now study full PNPF (with steric, correlation, and water NP effects) simulations of the GA channel using the SMIB and SG methods. Fig. 4 is a comparison of the I-V curves obtained by PNPF (lines) and the experimental data (symbols) from Cole et al. [73] with bath  $K^+$  and  $Cl^-$  concentrations  $C^B = 0.1, 0.2, 0.5, 1$ , and 2 M and membrane potentials  $\Delta V = V_i - V_o = 0, 50, 100, 150$ , and 200 mV. The PNPF currents in pico ampere (pA) were obtained with only one adjustable parameter, namely, the reduction parameter  $\theta$  in the pore diffusion coefficients  $\theta D_i^B$  for all particle species, while all physical parameters in Table I were kept fixed throughout simulations. This kind of reduction parameter has been used in all previous PNP papers and is necessary in continuum simulations when compared with MD, BD, or experimental data because there is abundant qualitative evidence that the diffusion coefficient in channels is much smaller than in bulk, but quantitative estimates are not available, as well described by Gillespie in [56] including Appendix and supporting material. In principle, all experimental data can be fitted by adjusting this parameter. For the PNPF currents at all  $C^B$  and  $\Delta V$  in Fig. 4, we chose  $\theta = 1/4.7$  which agrees with the range  $1/3$  to  $1/10$  obtained by many MD simulations of various channel models [24,74,75], indicating that the steric, correlation, and water NP properties have made PNPF simulations more closer (realistic) to MD simulations than previous PNP simulations for which the parameter  $\theta$  differs from MD values by an order to several orders of magnitude [24].

Furthermore, PNPF can also provide more physical properties that have not been observed by previous PNP models such as the variation of electric permittivity (dielectric function  $\tilde{\epsilon}(\mathbf{r})$  in Fig. 5) and water density ( $C_{H_2O}(\mathbf{r})$  in Fig. 6) from bath to channel pore. Together with the electric ( $\phi(\mathbf{r})$  in Fig. 7) and steric ( $S^{\text{trc}}(\mathbf{r})$  in Fig. 8) potentials,  $K^+$  ions (in Fig. 9) are subject not only to the electric field  $-\nabla\phi(\mathbf{r})$  but also to the steric (entropic) field  $\nabla S^{\text{trc}}(\mathbf{r})$  as described in Eq. (10). These fields change with the variations of water density, other ion concentrations, voids  $\Gamma(\mathbf{r})$ , and dielectric function  $\tilde{\epsilon}(\mathbf{r})$  at any location  $\mathbf{r}$  in the solvent domain  $\Omega_s$ . For example, the magnitude of electric fields

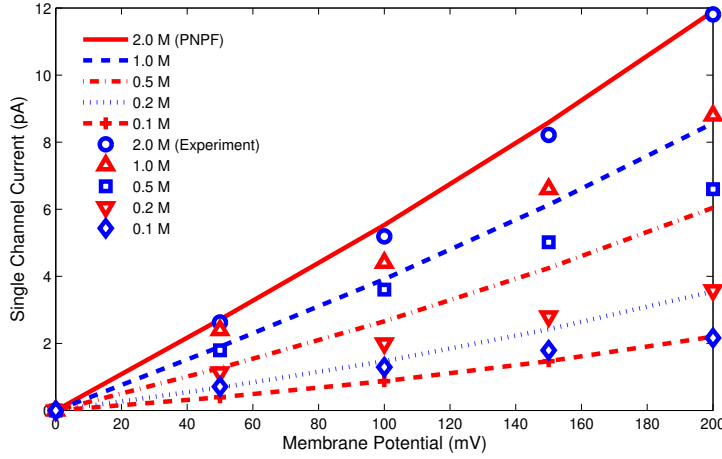


Fig. 4. A comparison of PNPf (lines) and experimental [73] (symbols) I-V results with bath  $K^+$  and  $Cl^-$  concentrations  $C^B = 0.1, 0.2, 0.5, 1, 2$  M and membrane potentials  $\Delta V = 0, 50, 100, 150, 200$  mV.

modified by the dielectric function  $\tilde{\epsilon}(\mathbf{r})$  can be as large as  $(80 - 50)/80 = 37.5\%$  of that by the constant permittivity  $80\epsilon_0$  for the bath condition  $C^B = 2$  M with the membrane potential 200 mV as shown in Fig. 5. The dielectric function in  $\tilde{\epsilon}(\mathbf{r})\epsilon_0$  was calculated by

$$\tilde{\epsilon}(\mathbf{r}) = \epsilon_m + C_{H_2O}(\mathbf{r})(\epsilon_w - \epsilon_m)/C_{H_2O}^B \quad (31)$$

using the water density function  $C_{H_2O}(\mathbf{r})$  as proposed in [76]. The protein is most negatively charged around  $z = 13$  Å, where the pore is very narrow (about 1.6 Å in radius) so that it is most crowded (most negative  $S^{trc}(\mathbf{r}) = \ln \frac{\Gamma(\mathbf{r})}{\Gamma^B}$  in Fig. 8) there. The size effect of all particle species is clearly manifested by the steric function  $S^{trc}(\mathbf{r})$  in PNPf. These results provide one of the most comprehensive simulations on ion transport in real proteins using continuum models that we know of.

The incompressibility of water and the mass conservation are important physical properties that can be used to further verify continuum results. MD simulations have shown that the GA channel can be occupied by two  $K^+$  ions at moderately high concentration [77,78]. In Fig. 10(a), we observe that a total of 8 particles (water molecules plus  $K^+$  ions) in the channel pore is conserved by PNPf but not by PNP as  $[KCl]$  increases from 0 to 2 M. The pore volume is determined by a length of 22 Å (from 11 to 33 Å in the channel axis in Fig. 9) and radii varying from 1.466 to 2.343 Å along the axis (not shown). The PNPf water density profiles in Fig. 6 show that water molecules adjust self-consistently their configurations to accommodate  $K^+$  ions (Fig. 9) in the two binding sites near the mouths of the channel as  $[KCl]$  increases. The complementary profiles of water and  $K^+$  in Figs. 6 and 9 illustrate a continuum picture of six water molecules separating two  $K^+$  ions in single file [78]. Figs.

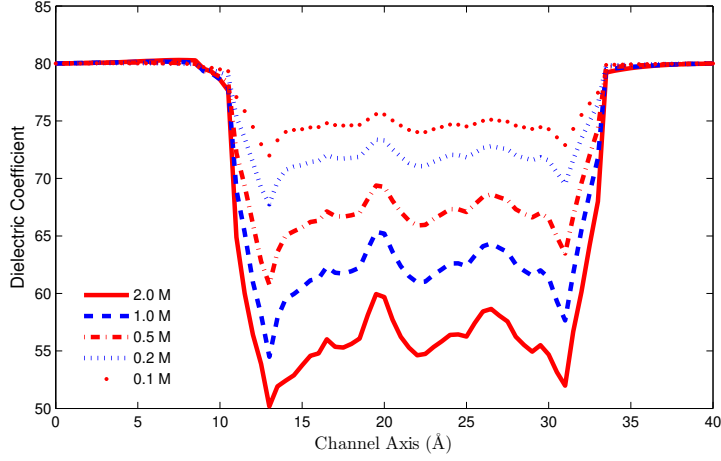


Fig. 5. The averaged dielectric function  $\tilde{\epsilon}(\mathbf{r})$  profiles at each cross section along the pore axis with  $C^B = 0.1, 0.2, 0.5, 1, 2$  M and  $\Delta V = 200$  mV. Figs. 5.3 – 5.6 are obtained with the same averaging method,  $C^B$ , and  $\Delta V$ .

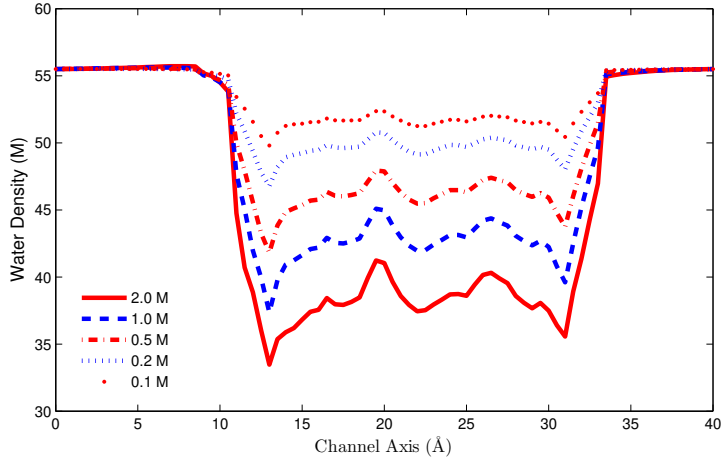


Fig. 6. The averaged water density  $C_{H_2O}(\mathbf{r})$  profiles.

10(a) and 10(b) also illustrate the saturation of ions and currents, respectively, as  $[KCl]$  increases. Note that PNP yields less  $K^+$  ions (and hence currents) since the constant permittivity  $\epsilon = \epsilon_w \epsilon_0$  in Eq. (8) for PNP (with  $l_c = 0$ ) is larger than the variable permittivity  $\tilde{\epsilon}(\mathbf{r})\epsilon_0$  obtained by Eq. (31) for PNPF (with  $l_c \neq 0$ ) as shown in Fig. 5, i.e., larger  $\epsilon$  results in smaller charge density  $\rho$  (fewer ions) for the same  $\phi$ .

Therefore, the mass conservation and saturation results in Fig. 10 and the PNPF current results in Fig. 4 with the MD compatible parameter  $\theta = 1/4.7$  appear to justify the approximation formula (31) for calculating the variable  $\tilde{\epsilon}(\mathbf{r})$  that is an output for illustration. We emphasize that in our treatment, unlike most treatments of channels, dielectric and polarization effects are operators that are outputs of the calculations. They are not assumed as constants.

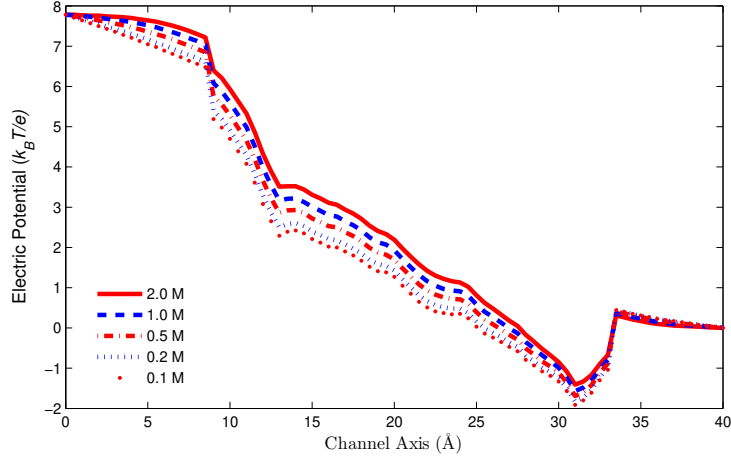


Fig. 7. The averaged electric potential  $\phi(\mathbf{r})$  profiles.

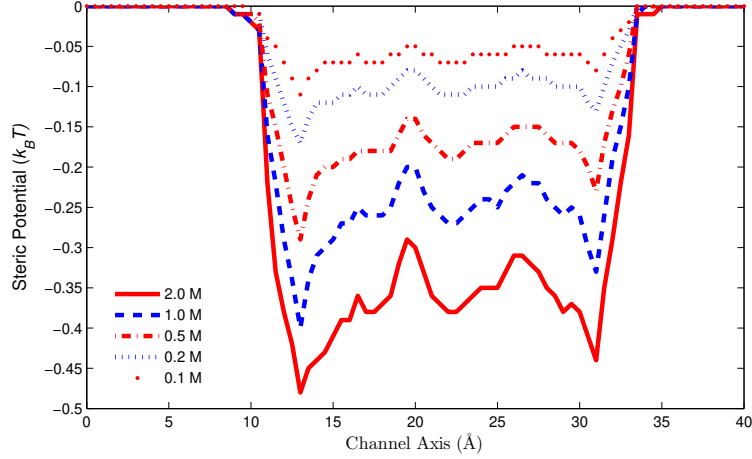


Fig. 8. The averaged steric potential  $S^{\text{trc}}(\mathbf{r})$  profiles.

The polarization effects of water are actually approximated by the dielectric operator  $\hat{\epsilon} = \epsilon_s(1 - l_c^2 \nabla^2)$  in Eq. (8) not by  $\tilde{\epsilon}(\mathbf{r})$ . Obviously, the polarization effects (or equivalently the correlation effects of ions in PNPF) play a crucial role in very narrow channels that are more challenging to describe by classical PNP models or even by all-atom MD simulations as the current MD force fields do not include the electronic polarization effects [79,80]. Of course, the single-file picture by PNPF is still far from that by MD [78] due to inevitable averaging effects of numerous atoms in the system. Nevertheless, the electrostatic, steric, and dielectric fields produced by PNPF may improve MD as well as continuum simulations in future studies.

We make a final remark about the nonlinear iteration method for GA simulations. The two relaxation parameters of the SOR-like scheme in Algorithm 1 were set to  $\omega_{\text{PF}} = 0.3$  and  $\omega_{\text{PNPF}} = 0.5$  for all above results. The number of iterations for each PNPF I-V data point in Fig. 4 is given in Table IV.



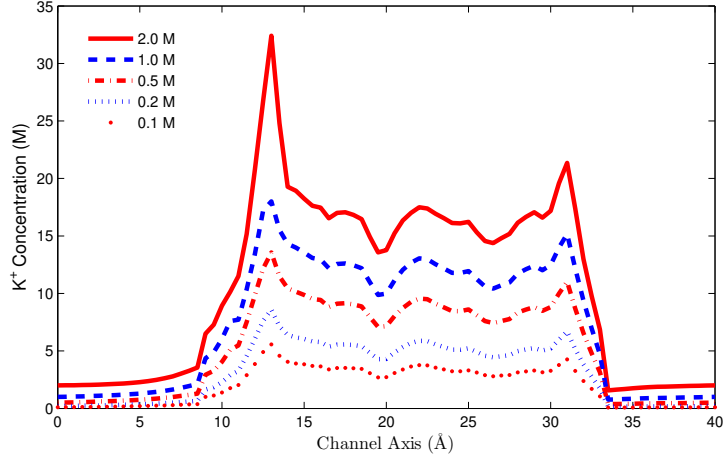


Fig. 9. The averaged  $K^+$  concentration  $C_{K^+}(\mathbf{r})$  profiles.

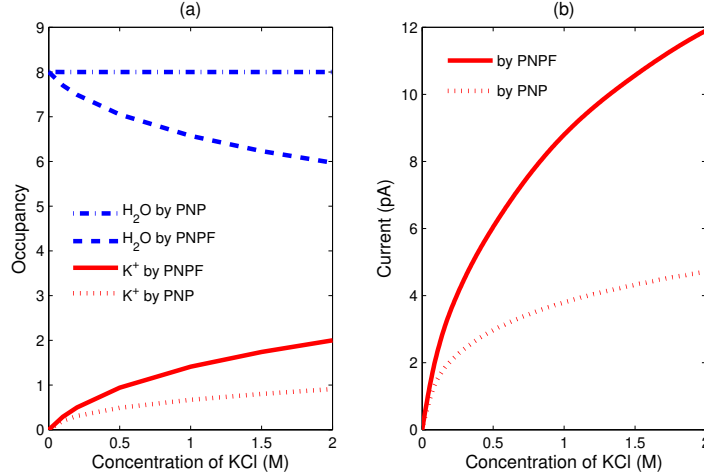


Fig. 10. (a) Occupancy of  $H_2O$  and  $K^+$  in the GA channel pore by PNPF and PNP as  $[KCl]$  increases from 0 to 2 M. The total number of  $H_2O$  and  $K^+$  in the pore is 8 [77], which is conserved by PNPF but not by PNP (without steric and correlation effects). (b) Currents by PNPF and PNP at  $\Delta V = 200$  mV. PNP underestimates the currents.

We do not need to solve NP equations when  $\Delta V = 0$ . Iterations for solving PF1 and PF2 in Steps 3 and 4 in Algorithm 1 increase with increasing bath concentrations as shown in the table. Iterations for solving  $K^+$ ,  $Cl^-$ , and  $H_2O$  NP equations and then PF1 and PF2 in Steps 6, 7, 8 are all about 22 for  $C^B = 0.1$  to 1 M when  $\Delta V \neq 0$ . These numbers are more steady and less than those in [22] (see Table 7 in that paper). For  $C^B = 2$  M, iterations increase with increasing  $\Delta V$  as those in [22]. Note that the relaxation parameter was set to different values for the first 3 steps in [22] whereas  $\omega_{PF}$  and  $\omega_{PNPF}$  were fixed throughout here.

TABLE IV. SOR Iterations

$C^B \backslash \Delta V$	0mV	50	100	150	200
0.1M	22	22	22	22	22
0.2	30	22	22	22	22
0.5	45	21	22	22	22
1.0	61	21	21	21	21
2.0	78	34	38	43	49

## B. Calcium Channel

The calcium channel operates very delicately in physiological and experimental conditions as it shifts its exquisitely tuned conductance from  $\text{Na}^+$ -flow, to  $\text{Na}^+$ -blockage, and to  $\text{Ca}^{2+}$ -flow when bath  $\text{Ca}^{2+}$  varies from trace to high concentrations. In [66], 19 extracellular solutions and 3 intracellular solutions were studied experimentally, in which the range of  $[\text{Ca}^{2+}]_o$  is  $10^8$ -fold from  $10^{-10.3}$  to  $10^{-2}$  M.

PNPF results are in accord with the experimental data in [66] as shown in Fig. 11 under only the same salt conditions of NaCl and  $\text{CaCl}_2$  in pure water, without considering other bulk salts in experimental solutions. With  $[\text{Na}^+]_i = [\text{Na}^+]_o = 32$  mM and  $[\text{Ca}^{2+}]_i = 0$ , the membrane potential is fixed at  $-20$  mV ( $V_o = 0$  and  $V_i = -20$  mV) throughout, as assumed in Fig. 11 of [66] for all single-channel currents (in femto ampere fA) recorded in the experiment. The small circles in Fig. 11 denote the experimental currents from Fig. 11 of [66] and the plus signs denote the total currents calculated by PNPF, where the partial  $\text{Ca}^{2+}$  and  $\text{Na}^+$  currents are denoted by the solid and dotted line, respectively. These two ionic currents show the anomalous fraction effect of the channel at nonequilibrium. The reduction parameter in  $\theta D_i$  was set to  $\theta = 0.1$  and all physical parameters in Table I were kept fixed throughout.

Solution profiles of calcium channel are quite different from those of GA channel as shown in Figs. 12 (dielectric function  $\tilde{\epsilon}(\mathbf{r})$ ), 13 (water density  $C_{\text{H}_2\text{O}}(\mathbf{r})$ ), 14 (electric potential  $\phi(\mathbf{r})$ ), 15 (steric potential  $S^{\text{trc}}(\mathbf{r})k_B T$ ), and 16 (scaled flux density  $|\mathbf{J}_{\text{Ca}^{2+}}(\mathbf{r})|$ ). Fig. 12 displays the combined effects of correlation, polarization, and screening in this highly inhomogeneous electrolyte by means of the dielectric function  $\tilde{\epsilon}(\mathbf{r})$  in which water (Fig. 13) plays a more profound role than that of GA channel as the water density is dramatically reduced from 55.5 M in the bath to almost 0 in the binding site when  $[\text{Ca}^{2+}]_o = 10^{-2}$  M.

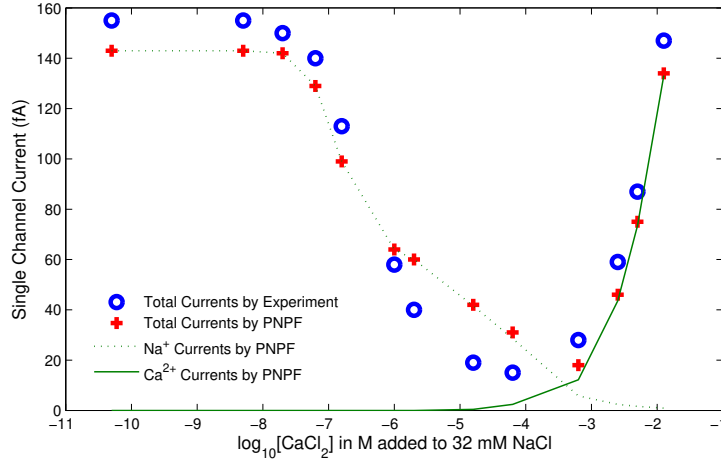


Fig. 11. Single channel inward current in femto ampere (fA) plotted as a function of  $\log_{10}[\text{Ca}^{2+}]_o$ . Experimental data of [66] are marked by small circles and PNPf data are denoted by the plus sign and lines.

Water is not allowed to occupy the binding site because  $\text{Ca}^{2+}$  occupies it in this bath condition and the 8  $\text{O}^{1/2-}$  ions in the EEEE locus are electrically attracted toward the binding  $\text{Ca}^{2+}$  as illustrated by Fig. 2(a). The EEEE locus is very hydrophobic in this condition. Without using the atomic properties of water and ions *inside* the solvent domain  $\Omega_s$  like those in (22)-(24), continuum models are not likely to produce results like Figs. 12 and 13. Mathematically, the Dirichlet condition  $\phi(\mathbf{r}) = \tilde{\phi}_b(\mathbf{r})$  in the interior of  $\Omega_s$ , i.e.  $\overline{\Omega}_{\text{Bind}} \subset \Omega_s$  in (27), is crucially important to connect the continuum Poisson-Fermi model (4) in  $\Omega_s \setminus \overline{\Omega}_{\text{Bind}}$  to the molecular (Coulomb) model (22)-(24) in  $\overline{\Omega}_{\text{Bind}}$ . From the binding formula (24), the pore radius is enlarged by the binding  $\text{Na}^+$  when  $[\text{Ca}^{2+}]_o$  decreases from  $10^{-2}$  to  $10^{-7.2}$  M, i.e.,  $\text{Na}^+$  occupancy ( $O_1$  in (26)) increases. The enlarged radius allows more space for water molecules in the channel pore as shown in Fig. 13.

**Novel Features.** The steric potential profiles shown in Fig. 15 represent the novelty of the PNPf theory. All effects of volume exclusion, interstitial void, configuration entropy, short range interactions, correlation, polarization, screening, and dielectric response of this nonideal system are described by the steric functional  $S^{\text{trc}}(\mathbf{r})$ . The steric potential in the binding region decreases drastically from  $-1.30$  to  $-10.34 k_B T$  as  $[\text{Ca}^{2+}]_o$  increases from  $10^{-7.2}$  to  $10^{-2}$  M. However, the electric potential remains almost unchanged as shown in Fig. 14 following the linear occupancy model (26). In physiological bath conditions  $[\text{Ca}^{2+}]_o = 10^{-2} \sim 10^{-3}$  M, Fig. 13 shows that the region containing the binding site with the length about  $10 \text{ \AA}$  is very dry (hydrophobic), which agrees with the recent crystallographic analysis [67] of the  $\text{Ca}^{2+}$  binding site of the related protein NCX with the EETT locus showing a hydrophobic patch (also about  $10 \text{ \AA}$  in length) formed by the conserved Pro residues. The hydrophobicity near the binding site in our model is described by the continuous water

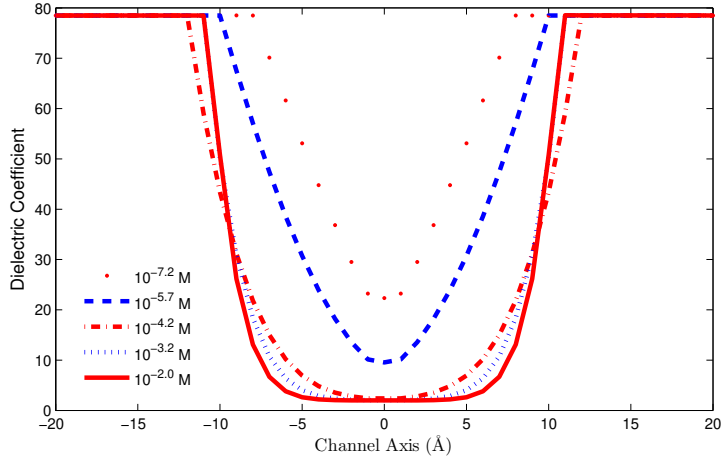


Fig. 12. The averaged dielectric function  $\tilde{\epsilon}(\mathbf{r})$  profiles at each cross section along the pore axis for various  $[\text{Ca}^{2+}]_o$  ranging from  $10^{-7.2}$  M to  $10^{-2}$  M. All the following figures are obtained with the same averaging method and the same range of  $[\text{Ca}^{2+}]_o$ .

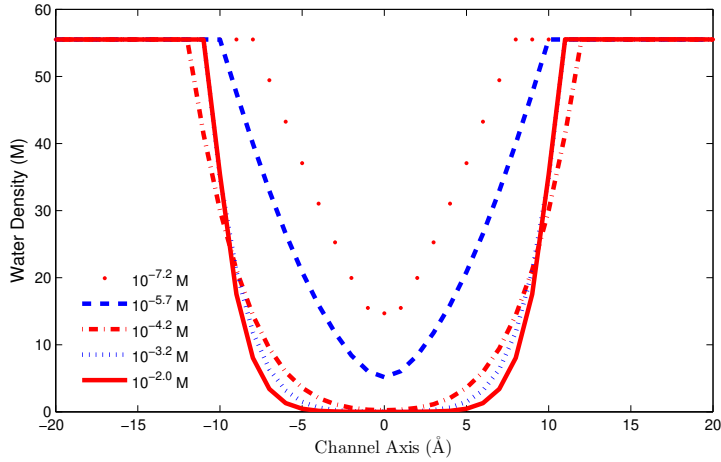


Fig. 13. The averaged water density  $C_{\text{H}_2\text{O}}(\mathbf{r})$  profiles.

density function  $C_{\text{H}_2\text{O}}(\mathbf{r})$  via the continuous steric function  $S^{\text{trc}}(\mathbf{r})$ , namely, the Fermi distribution  $C_{\text{H}_2\text{O}}(\mathbf{r}) = C_{\text{H}_2\text{O}}^{\text{B}} \exp(S^{\text{trc}}(\mathbf{r}))$  in (5). At  $[\text{Ca}^{2+}]_o = 10^{-2}$  M, the magnitude of the steric energy  $S^{\text{trc}} = -10.34 k_B T$  is comparable to that of the electrostatic energy  $\phi = -10.48 k_B T/e$ . This surprisingly large energy due only to the steric effect has not been quantified and observed by other continuum methods in  $\text{Ca}_V$  channel modeling, as far as we know.

The variable steric potential with respect to bath concentrations as shown in Fig. 15 plays a similar role as the confinement potential in MC simulations for constraining the 8 mobile  $\text{O}^{1/2-}$  ions of protein glutamates in a filter [59]. These are two different approaches to modeling the flexible glutamates and the steric effect of ions. The excluded volumes of electrolyte and glutamate ions are *explicitly given* as an *input* in MC simulations by using the confinement

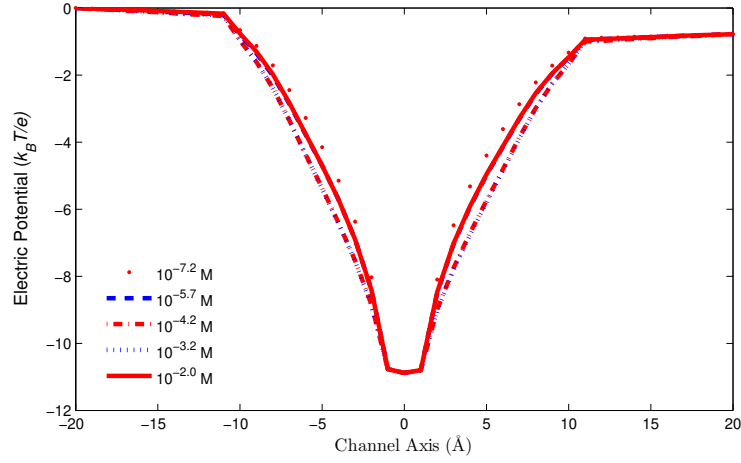


Fig. 14. The averaged electric potential  $\phi(\mathbf{r})$  profiles.

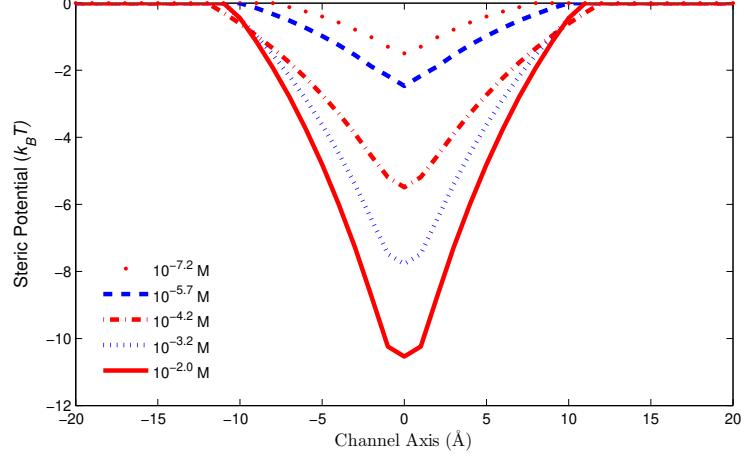


Fig. 15. The averaged steric potential  $S^{\text{trc}}(\mathbf{r})$  profiles.

potential in a *fixed filter* whereas the volumes are *implicitly calculated* in PNPF simulations and are *outputs* that describe the steric potential in a *variable binding site*. We had difficulties obtaining nonequilibrium results as those in Fig. 11 in our early attempt to use a fixed confinement potential in a fixed filter partly because the confinement potential would generate large artificial electric fields near the boundary of the filter in continuum setting. It is also difficult to incorporate the confinement potential into the flux density in Eq. (10) since the confinement potential is fixed and cannot not be explicitly decomposed to the electrostatic and non-electrostatic parts the way  $\phi$  and  $S^{\text{trc}}$  do in (10). These difficulties are typical of inconsistent calculations. Imposing potentials (whether in simulations or theories) requires injection of charge and mass that is not present in the real system. The injection occurs at a sensitive part of the system, the selectivity filter. The approach here avoids these difficulties.

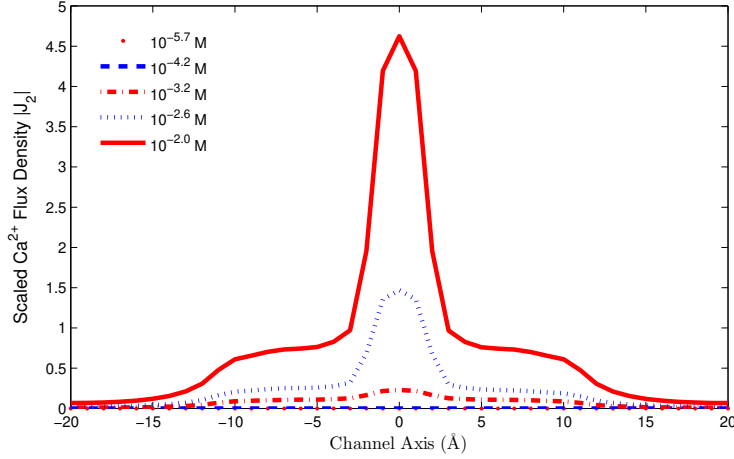


Fig. 16. The averaged flux density  $|\mathbf{J}_{\text{Ca}^{2+}}(\mathbf{r})|$  profiles.

As observed from Fig. 11, ionic transport is blocked by the competition between  $\text{Na}^+$  and  $\text{Ca}^{2+}$  ions in the range  $[\text{Ca}^{2+}]_o = 10^{-5.7} \sim 10^{-4.2}$  M. In this blocking range, the corresponding steric profiles in Fig. 15 are wider indicating that the water density or the void volume is more evenly distributed. From Fig. 11, we observe that  $\text{Ca}^{2+}$  currents increase dramatically when  $[\text{Ca}^{2+}]_o$  increases from  $10^{-3.2}$  to  $10^{-2}$  M in the physiological mM range of the channel, so does the corresponding flux density as shown in Fig. 16.

**Numerical Verification.** All the above results were obtained by using the standard FD method (see [45] for instance) for the Poisson-Fermi equations (6)-(7) and the Scharfetter-Gummel method (21) for the flux equation (9). We now provide more numerical details for the extended SG stability condition (18) and explain why the primitive method (12) fails. We first verify the SG method at equilibrium ( $\Delta V = V_o = V_i = 0$ ) for which the PNPF solution should agree with the PF solution as shown in Table V, where the averaged  $\text{Na}^+$  and  $\text{Ca}^{2+}$  concentrations in the filter (binding site) are denoted by  $C_1^F$  and  $C_2^F$ , respectively. Here, the approximate PF solution of  $C_i(\mathbf{r})$  in (5) is treated as an exact solution to justify the approximate PNPF solution. The PNPF concentrations agree quite well with the PF concentrations indicating that the SG method (21) works well. Note that  $C_1^F$  and  $C_2^F$  are all bounded by their respect maximum values 462.39 and 408.57 M at very large electrostatic potential  $\phi = -10.48$  in the filter, as guaranteed by the Fermi distribution (5). We use the SOR method [81] for solving all linear algebraic systems with the relaxation parameter taken to be 1.9. The error tolerance of the SOR linear solver is  $10^{-8}$  because the boundary bath condition  $[\text{Ca}^{2+}]_o$  for (21) is in the  $10^8$ -fold range. The error tolerance for solving each PDE in the PNPF model in Algorithm 2 is  $10^{-4}$ .

TABLE V. Verification of the SG method (21)

$[\text{Ca}^{2+}]$ in M	$0.9 \cdot 10^{-6}$	$10^{-5}$	$10^{-4}$	$10^{-3}$	$10^{-2}$
PF $C_1^F/C_2^F$	61.7/63.7	10.1/116.9	1.1/126.2	0.11/127.3	0.01/127.4
PNPF	61.7/63.4	10.1/116.1	1.1/126.2	0.11/127.3	0.01/127.4

**Primitive FD method fails.** We next look more closely into the numerics of the SG discretization concerning the SG condition (18) at nonequilibrium ( $\Delta V = -20$  mV) under the conditions as those in Fig. 11. In Table VI,  $-\beta_i \Delta \phi$  denotes the maximum difference of  $-\beta_i \phi(\mathbf{r})$  between all adjacent pairs of grid points in 3D, where the subscript  $i$  denotes the ionic species not the grid node. Since  $[\text{Ca}^{2+}]_o$  varies in the  $10^8$ -fold range, the maximum difference  $-\beta_i \Delta \phi$  varies in a range for each ionic species  $i$  as shown in the table. Moreover, the adjacent pair of grid points at which the maximum difference is obtained may differ for different NP equations. The other two maximum differences  $\Delta S^{\text{trc}}$  and  $-\beta_i \Delta \phi + \Delta S^{\text{trc}}$  are similarly defined. Note also that the three maximum differences may occur at different pairs of adjacent grid points with the mesh size  $h = 1$  Å even for the same NP equation.

TABLE VI. Checking the SG condition (18)

	$-\beta_i \Delta \phi$	$\Delta S^{\text{trc}}$	$-\beta_i \Delta \phi + \Delta S^{\text{trc}}$
NP1 ( $\text{Na}^+$ )	$2.43 \sim 2.79$	$0.34 \sim 1.75$	$1.16 \sim 2.51$
NP2 ( $\text{Ca}^{2+}$ )	$4.86 \sim 5.59$	$0.34 \sim 1.75$	$4.03 \sim 5.30$
NP3 ( $\text{Cl}^-$ )	$2.47 \sim 2.82$	$0.34 \sim 1.75$	$0.34 \sim 1.75$

From Table VI, we observe that the primitive FD method (12) violates the SG condition (18) for all NP1, NP2, and NP3 (without  $S^{\text{trc}}$ ) and for NP1 and NP2 (with  $S^{\text{trc}}$ ). The worst case of the violation occurs in the  $\text{Ca}^{2+}$  flux equation NP2 with or without  $S^{\text{trc}}$ , as analyzed in (17). Obviously, the primitive FD is not suitable for PNPF simulations on  $\text{Ca}_v$  channels. The SG not only delivers stable results for all equations in the PNPF model at all experimental conditions but also converges very rapidly in the nonlinear iteration.

## VI. CONCLUSION

The classical Scharfetter-Gummel (SG) method for semiconductor devices was extended to include the steric potential for biological ion channels in this paper. The steric potential — a key feature of the PNPF theory — represents a combination of various effects of volume exclusion, interstitial void, configuration entropy, short range interactions, correlation, polarization, screening,

and dielectric response in a complex fluid system of ion channel. The simplified matched interface and boundary (SMIB) method together with the SG method was shown to yield optimal convergence for a PNP model with exact solutions of the gramicidin A channel. The primitive finite difference method without SG was shown to lead to unphysical approximations for an L-type calcium channel due to the violation of the generalized SG condition presented here. Two algorithms based on the SMIB and multiscale methods have been presented for these two different types of channels depending on whether water is allowed to pass through the channel pore. Numerical results for both channels are in accord with the respective experimental results. Compared with previous PNP models, new physical details by PNPF such as water dynamics, dielectric function, voids, and steric energy in the system have been illustrated and discussed. The PNPF model differs from most channel models in several respects. It computes dielectric properties as an output that in fact vary with position and with experimental condition. It provides a fourth order partial differential equation to describe current flow, of the general Cahn-Hilliard type, which has a richness of behavior beyond the usual second order PNP description. Practically, it is important that PNPF is much easier to compute in three dimensions than other steric PNP models.

## ACKNOWLEDGEMENTS

This work was supported in part by the Ministry of Science and Technology of Taiwan under Grant No. 103-2115-M-134-004-MY2 to J.L.L and by the Bard Endowed Chair of Rush University Medical Center, held by B.E.

## References

- [1] H. K. Gummel, IEEE Trans. Elec. Dev. **11**, 163 (1964).
- [2] D. L. Scharfetter and H. K. Gummel, IEEE Trans. Elec. Dev. **16**, 64 (1969).
- [3] J. W. Slotboom, IEEE Trans. Elec. Dev. **20**, 669 (1973).
- [4] R. E. Bank, D. J. Rose, and W. Fichtner, IEEE Trans. Elec. Dev. **30**, 1031 (1983).
- [5] P. A. Markowich, C. A. Ringhofer, S. Selberherr, and M. Lentini, IEEE Trans. Elec. Dev. **30**, 1165 (1983).
- [6] S. Selberherr, *Analysis and Simulation of Semiconductor Devices* (Springer-Verlag, New York, 1984).
- [7] C. M. Snowden, *Semiconductor Device Modelling* (Peter Peregrinus Ltd., London, UK, 1988).
- [8] T. Kerkhoven, SIAM J. Sci. Statist. Comput. **9**, 48 (1988).



- [9] U. Ascher, P. Markowich, C. Schmeiser, H. Steinruck, and R. Weiss, SIAM J. Appl. Math. **49**, 165 (1989).
- [10] F. Brezzi, L. D. Marini, and P. Pietra, SIAM J. Numer. Anal. **26**, 1342 (1989).
- [11] C. Ringhofer and C. Schmeiser, SIAM J. Numer. Anal. **26**, 507 (1989).
- [12] N. R. Aluru, A. Raefsky, P. M. Pinsky, K. H. Law, R. J. G. Goossens, and R. W. Dutton, Comput. Methods Appl. Mech. Engrg. **107**, 269 (1993).
- [13] J. W. Jerome, SIAM Rev. **37**, 552 (1995).
- [14] M. G. Kurnikova, R. D. Coalson, P. Graf, and A. Nitzan, Biophys. J. **76**, 642 (1999).
- [15] A. E. Cárdenas, R. D. Coalson, and M. G. Kurnikova, Biophys. J. **79**, 80 (2000).
- [16] R.-C. Chen and J.-L. Liu, J. Comput. Phys. **189**, 579 (2003).
- [17] R. Pinnau, SIAM J. Numer. Anal. **42**, 1648 (2004).
- [18] R.-C. Chen and J.-L. Liu, J. Comput. Phys. **204**, 131 (2005).
- [19] R.-C. Chen and J.-L. Liu, J. Comp. Phys. **227**, 6266 (2008).
- [20] B. Lu, M. J. Holst, J. A. McCammon, and Y. C. Zhou, J. Comput. Phys. **229**, 6979 (2010).
- [21] N. A. Simakov and M. G. Kurnikova, J. Phys. Chem. B **114**, 15180 (2010).
- [22] Q. Zheng, D. Chen, and G.-W. Wei, J. Comp. Phys. **230**, 5239 (2011).
- [23] C. Sagui and T. A. Darden, Annu. Rev. Biophys. Biomol. Struct. **28**, 155 (1999).
- [24] T. W. Allen, S. Kuyucak, and S. H. Chung, Biophys. Chem. **86**, 1 (2000).
- [25] B. Corry, S. Kuyucak, and S.-H. Chung, Biophys. J. **78**, 2364 (2000).
- [26] C. N. Schutz and A. Warshel, Proteins: Structure, Function, and Bioinformatics **44**, 400 (2001).
- [27] W. Im and B. Roux, Biophys. J. **115**, 4850 (2001).
- [28] W. Im and B. Roux, J. Mol. Biol. **322**, 851 (2002).
- [29] S.-H. Chung and S. Kuyucak, Biochim. Biophys. Acta **1565**, 267 (2002).
- [30] S. Edwards, B. Corry, S. Kuyucak, and S.-H. Chung, Biophys. J. **83**, 1348 (2002).
- [31] G. V. Miloshevsky and P. C. Jordan, Trends in Neurosciences **27**, 308 (2004).
- [32] B. Roux, T. Allen, S. Berneche, and W. Im, Q. Rev. Biophys. **37**, 15 (2004).
- [33] C. Song and B. Corry, PLoS ONE **6**, e21204 (2011).

- [34] F. Fogolari, A. Brigo, and H. Molinari, *J. Mol. Recognit.* **15**, 377 (2002).
- [35] P. Graf, M. G. Kurnikova, R. D. Coalson, and A. Nitzan, *J. Phys. Chem. B* **108**, 2006 (2004).
- [36] R. D. Coalson and M. G. Kurnikova, *IEEE Trans. Nanobio.* **4**, 81 (2005).
- [37] B. Eisenberg, *J. Phys. Chem. C* **114**, 20719 (2010).
- [38] B. Eisenberg, in *Advances in Chemical Physics*, edited by S. A. Rice (John Wiley & Sons, Inc. Vol. 148, 2011), p. 77.
- [39] B. Eisenberg, *SIAM News* **45**, 11 (2012).
- [40] G.-W. Wei, Q. Zheng, Z. Chen, and K. Xia, *SIAM Rev.* **54**, 699 (2012).
- [41] B. Eisenberg, *Biophys. J.* **104**, 1849 (2013).
- [42] J.-L. Liu and B. Eisenberg, *J. Phys. Chem. B* **117**, 12051 (2013).
- [43] J.-L. Liu and B. Eisenberg, *J. Chem. Phys.* **141**, 22D532 (2014).
- [44] W. Geng, S. Yu, and G. Wei, *J. Chem. Phys.* **127**, 114106 (2007).
- [45] J.-L. Liu, *J. Comp. Phys.* **247**, 88 (2013).
- [46] B. Hille, *Ionic Channels of Excitable Membranes* (Sinauer Associates Inc., Sunderland, MA, 2001).
- [47] N. F. Mott, The theory of crystal rectifiers, *Proc. Roy. Soc. A* **171**, 27 (1939).
- [48] W. A. Sather and E. W. McCleskey, *Annu. Rev. Physiol.* **65**, 133 (2003).
- [49] C. D. Santangelo, *Phys. Rev. E* **73**, 041512 (2006).
- [50] M. Z. Bazant, B. D. Storey, and A. A. Kornyshev, *Phys. Rev. Lett.* **106**, 046102 (2011).
- [51] S. M. Hou and X.-D. Liu, *J. Comput. Phys.* **202**, 411 (2005).
- [52] D. P. Chen, V. Barcilon, and R. S. Eisenberg, *Biophys. J.* **61**, 1372 (1992).
- [53] R. Eisenberg and D. Chen, *Biophys. J.* **64**, A22 (1993).
- [54] R. S. Eisenberg, M. M. Kłosek, and Z. Schuss, *J. Chem. Phys.* **102**, 1767 (1995).
- [55] S. Furini, F. Zerbetto, and S. Cavalcanti, *Biophys. J.* **91**, 3162 (2006).
- [56] D. Gillespie, *Biophys. J.* **94**, 1169 (2008).
- [57] R. P. Feynman, R. B. Leighton, and M. Sands, *The Feynman Lectures on Physics, Volume II, Mainly Electromagnetism and Matter* (Addison-Wesley Publishing Co., New York, 1963).
- [58] D. Boda, M. Valiskó, D. Henderson, B. Eisenberg, D. Gillespie, and W. Nonner, *J. Gen. Physiol.* **133**, 497 (2009).

- [59] H. M. Berman et al., Acta Cryst. **D58**, 899 (2002).
- [60] A. Shrake and J. A. Rupley, J. Mol. Biol. **79**, 351 (1973).
- [61] B. Nadler, U. Hollerbach, and R. S. Eisenberg, Phys. Rev. E **68** (2003) 021905.
- [62] D. Boda, D. D. Busath, B. Eisenberg, D. Henderson, and W. Nonner, Phys. Chem. Chem. Phys. **4**, 5154 (2002).
- [63] D. Boda, W. Nonner, M. Valiskó, D. Henderson, B. Eisenberg, and D. Gillespie, Biophys. J. **93**, 1960 (2007).
- [64] G. M. Lipkind and H. A. Fozzard, Biochem. **40**, 6786 (2001).
- [65] J.-L. Liu and B. Eisenberg, J. Chem. Phys. **141**, 075102 (2014).
- [66] W. Almers and E. W. McCleskey, J. Physiol. **353**, 585 (1984).
- [67] J. Liao et al., Science **335**, 686 (2012).
- [68] D. A. Doyle et al., Science **280**, 69 (1998).
- [69] M. Liao, E. Cao, D. Julius, and Y. Cheng, Nature **504**, 107 (2013).
- [70] L. Tang, L. Tang, T. M. G. El-Din, J. Payandeh, G. Q. Martinez, T. M. Heard, T. Scheuer, N. Zheng, and W. A. Catterall, Nature **505**, 56 (2014).
- [71] T. J. Dolinsky, P. Czodrowski, H. Li, J. E. Nielsen, J. H. Jensen, G. Klebe, and N. A. Baker, Nucleic Acids Res. **35**, W522 (2007).
- [72] U. Hollerbach, D.-P. Chen, and R. S. Eisenberg, J. Scient. Comput. **16**, 373 (2001).
- [73] C. D. Cole, A. S. Frost, N. Thompson, M. Cotten, T. A. Cross, and D. D. Busath, Biophys. J. **83**, 1974 (2002).
- [74] A. Mamonov, R. D. Coalson, A. Nitzan, and M. G. Kurnikova, Biophys. J. **84**, 3646 (2003).
- [75] G. R. Smith and M. S. P. Sansom, Biophys. J. **75**, 2767 (1998).
- [76] B. Lu and J. A. McCammon, Chem Phys Lett. **451**, 282 (2008).
- [77] B. Roux, B. Prod'homme, and M. Karplus, Biophys. J. **68**, 876 (1995).
- [78] B. Roux, Acc. Chem. Res. **35**, 366 (2002).
- [79] T. Baştuğ and S. Kuyucak, Biophys. J. **90**, 3941 (2006).
- [80] D. Bucher and S. Kuyucak, Chem. Phys. Lett. **477**, 207 (2009).
- [81] G. Golub and C. van Loan, *Matrix Computations* (The Johns Hopkins University Press 1996).